

The winds of hydrogen-rich central stars of planetary nebulae

J. E. Herald^{*} and L. Bianchi^{*}

Department of Physics and Astronomy, The Johns Hopkins University, 3400 North Charles Street, Baltimore, MD 21218, USA

Accepted 2011 June 24. Received 2011 June 14; in original form 2011 January 10

ABSTRACT

We have modelled far-UV, UV and optical spectra of a sample of 10 hydrogen-rich central stars of planetary nebulae (CSPN) using stellar atmosphere codes to derive their photospheric and wind parameters. The resulting stellar temperatures range from 40 to 120 kK, well spanning the CSPN evolutionary phase and allowing certain trends to be discerned. In particular, an inhomogeneous wind structure and X-ray emission in the wind are required to match spectral diagnostic lines in many cases. For the majority of the sample, a wind clumping factor of $0.1 \leq f \leq 0.04$ is derived (mainly from the P v $\lambda\lambda 1118, 28$ and O v $\lambda 1371$ lines). Such factors correspond to clump densities of ~ 10 – 25 times that of the smooth wind density, with resulting mass-loss rates one-third to one-fifth the smooth wind values, which is of significant consequence to nebular dynamics, stellar and galactic evolution. Furthermore, we find clumping to begin at small radii ($\sim 1.2 R_*$), as has been found when modelling the winds of (massive) O stars. The inclusion of X-ray fluxes, presumably from shocks, in the model atmosphere calculations is found to improve the fit of the O v i $\lambda\lambda 1032, 38$ line (and other features) for stars with $55 \leq T_{\text{eff}} \leq 80$ kK, and to be absolutely necessary to match this feature for the coolest stars in our sample ($T_{\text{eff}} \lesssim 45$ kK). These findings suggest that shocks originating from line-driven wind instabilities leading to the formation of clumped winds and X-rays may be a common characteristic of CSPN, as has been found for the winds of massive O-type stars.

We also find interesting results for some individual stars. NGC 1360 ($T_{\text{eff}} \simeq 105$ kK) displays the signature of a (previously undetected) weak stellar wind in its O v i 1032, 38 profile, and probably has the lowest mass-loss rate ($\dot{M} \lesssim 1 \times 10^{-10} M_{\odot} \text{ yr}^{-1}$) of any known CSPN. In contrast, we find the wind terminal velocity of NGC 2392 ($T_{\text{eff}} \simeq 45$ kK) to be $v_{\infty} \simeq 300 \text{ km s}^{-1}$, one of the slowest CSPN wind known, probably related to its subsolar metallicity. We have included in the model calculations many elements and high-ionization species previously neglected in analyses of this type, providing additional wind diagnostics such as Ne v i i $\lambda 973$ and Ar v i i $\lambda 1064$. The effects of including these as well as other line-blanking elements are discussed.

Key words: stars: abundances – stars: AGB and post-AGB – stars: atmospheres – white dwarfs – planetary nebulae: general – ultraviolet: stars.

1 INTRODUCTION

Stars with progenitor masses of $M_{\text{init}} \lesssim 8 M_{\odot}$ eject surface material throughout the asymptotic giant branch (AGB) phase, which forms a circumstellar nebula. Upon leaving the AGB phase, they evolve at roughly constant luminosity across the Hertzsprung–Russell (HR) diagram, eventually reaching temperatures high enough to ionize the

surrounding material, creating what has become known as a ‘planetary nebula’. Stars in this central star of planetary nebulae (CSPN) phase typically have surface temperatures ranging from 30 to 200 kK, stellar winds with terminal velocities of 300–4000 km s^{-1} and mass-loss rates of $1 \times 10^{-9} \lesssim \dot{M} \lesssim 1 \times 10^{-6} M_{\odot} \text{ yr}^{-1}$. Eventually, the wind fades, nuclear-core burning ceases and the star transitions off the constant-luminosity phase on to the white dwarf cooling sequence.

CSPN can be roughly split into two categories based on their surface abundances: ‘hydrogen-rich’ and ‘hydrogen-deficient’. The

^{*}E-mail: herald@pha.jhu.edu (JEH); bianchi@pha.jhu.edu (LB)

Table 1. Sample stars and spectral types.

| Star | PN G | SpType | RA (J2000) | Dec. (J2000) | v_{rad} (km s ⁻¹) | Dist. (kpc) | v_{exp} (km s ⁻¹) | Diam. (arcsec) | Shape |
|----------|------------|--------|---------------|-----------------|---|-------------------|---|-------------------|---------------------------|
| IC 2448 | 285.7–14.9 | O(H) | 09 07 06.3 | −69 56 30.7 | −24.0 | 1.38 ¹ | 12 | 9 | Elliptical ² |
| IC 4593 | 025.3+40.8 | O(H) | 16 11 44.5 | +12 04 17.1 | 22.0 | ? | 12 | 13 | Round ³ |
| LSS 1362 | 273.6+06.1 | O(H) | 09 52 44.5 | −46 16 51 | −2.7 ⁴ | ? | ? | 90 | Ring ⁵ |
| NGC 1360 | 220.3–53.9 | O(H) | 03 33 14.6 | −25 52 18.0 | 41.8 | 0.35 ⁶ | 28 | 285 | filled Elliptical |
| NGC 1535 | 206.4–40.5 | O(H) | 04 14 15.8 | −12 44 22.0 | −3.2 | 2.31 ⁷ | 20 | 21 | Elliptical ² |
| NGC 2392 | 197.8+17.3 | O(H) | 07 29 10.8 | +20 54 42.5 | 84.2 | 1.60 ⁸ | 53 | 20 | Elliptical ³ |
| NGC 6058 | 064.6+48.2 | O(H) | 16 04 26.6 | +40 40 56.0 | 1 | ? | 27 | 23 | Bipolar core ³ |
| NGC 6210 | 043.1+37.7 | O(H) | 16 44 29.5 | +23 47 59.7 | −35.6 | 1.57 ⁹ | 21 | 16 | Elliptical ³ |
| NGC 6543 | 096.4+29.9 | Of-WR | 17 58 33.4 | +66 37 59.5 | −65.7 | 1.0 ¹⁰ | 20 | 19 | Elliptical ³ |
| NGC 7662 | 106.5–17.6 | O(H) | 23 25 53.6 | +42 32 06 | −12.2 | 0.8 ¹¹ | 28 | 17 | Elliptical ³ |

¹Palen et al. (2002); ²Pottasch & Bernard-Salas (2010); ³Stanghellini et al. (2006); ⁴Traulsen et al. (2005);

⁵Heber & Drilling (1984); ⁶Perryman et al. (1997); ⁷Ciardullo & Jacoby (1999); ⁸Terzian (1997); ⁹Hajian, Terzian & Bignell (1995);

¹⁰Reed et al. (1999); ¹¹Hajian & Terzian (1996).

H-rich class, which constitutes ~ 75 per cent of Galactic CSPN, has surface chemistries deviating little from solar values, and are thought to be either hydrogen or helium burning stars on their way to become DA-type white dwarfs. The H-deficient stars show enhanced surface abundances of He, C, O and Ne, and are thought to be in a post-helium flash, helium burning phase destined to become DO-type white dwarfs (see Werner & Herwig 2006 for a review).

The far-UV (~ 900 – 1200 Å) and UV (~ 1200 – 3300 Å) wavelength ranges are particularly useful for studying hot CSPN as they emit the bulk of their observable flux in this range, and, as the wind fades, the strongest wind lines are seen at these wavelengths (Koesterke, Dreizler & Rauch 1998; Herald, Bianchi & Hillier 2005; Bianchi 2011). Furthermore, diagnostics known to be sensitive to wind shocks such as O VI $\lambda\lambda 1032, 38$ and N V $\lambda\lambda 1238, 42$ lie in this regime. These winds are thought to be driven by radiation pressure, the same mechanism responsible for the winds of Population I O stars and Wolf–Rayet (WR) stars. Determining the stellar parameters of stars with appreciable winds is not trivial, as the presence of a wind alters the structure in the atmosphere compared to the hydrostatic case, necessitating sophisticated stellar atmosphere codes.

There have been a number of studies where modern stellar atmosphere plus wind codes have been used to analyse far-UV spectra of Galactic H-deficient CSPN (e.g. Herald & Bianchi 2004b; Werner et al. 2004; Bianchi & Herald 2007; Marcolino et al. 2007; Keller et al. 2011). Herald & Bianchi (2004a, 2007) analysed *Far Ultraviolet Spectroscopic Explorer* (*FUSE*) spectra of CSPN in the Magellanic Clouds. However, there are few examples where these codes have been applied to analyse high-resolution far-UV spectra of Galactic H-rich CSPN (one example is NGC 1535 by Herald & Bianchi 2004b). In this work, we model the far-UV *FUSE* spectra (in conjunction with UV and optical spectra) of a sample of 10 H-rich Galactic stars using modern stellar atmospheres codes. These models include many atomic elements neglected in previous analyses of this type. The stars are found to span the temperature range 40–120 kK, spanning a large fraction of the CSPN evolutionary phase.

This paper is organized as follows. The observations and data reduction are described in Section 2. Our models and parameter determinations are described in Section 3. Individual object results are presented in Section 4. The implications of our results are discussed in Section 5 and our conclusions in Section 6.

2 SAMPLE, OBSERVATIONS AND REDUCTION

Our sample objects and spectral types are listed in Table 1, along with radial velocities and distances taken from the literature as well as nebular characteristics (diameters and [O III] expansion velocities from Acker et al. 1992). Throughout this paper, presented observed spectra have been shifted into the rest frame of the star using the radial velocities from this table.

We used far-UV spectra taken with *FUSE* and UV spectra ($\gtrsim 1185$ Å) taken with the *Hubble Space Telescope's* (*HST*) Space Telescope Imaging Spectrograph (STIS) and with the *International Ultraviolet Explorer* (*IUE*) (summarized in Table 2). All far-UV and UV data were retrieved from the Multimission Archive at the Space Telescope Science Institute.

Optical spectra (resolution ~ 2.2 Å) for NGC 2392, 1360, 1535 and LSS 1362 have been kindly provided by H. Bond and are described in Afšar & Bond (2005). Optical spectra for IC 4593, NGC 6210, 6058 (resolution ~ 0.6 Å) have been kindly provided by O. DeMarco and are described in De Marco et al. (2004). She has also provided an unpublished 1996 optical spectrum for NGC 6543 (resolution ~ 1.5 Å) taken during the 1996 Isaac Newton Telescope (INT) run described in Crowther, De Marco & Barlow (1998). Many of these spectra show a combination of stellar absorption lines and nebular emission lines. Depending on the resolution, nebular contamination, while obscuring the line cores, may leave the line wings unaffected.

2.1 FUSE data

FUSE covers the wavelength range 905–1187 Å at a spectral resolution of $R \approx 20000$ (~ 15 km s⁻¹). The instrument is described by Moos et al. (2000). *FUSE* collected light concurrently in four different channels (LiF1, LiF2, SiC1 and SiC2), each of which is divided into two segments (A and B) recorded by two detectors, covering different subsets of the above range with some overlap. All of the utilized observations were taken through *FUSE's* Low Resolution Aperture (LWRS; 30×30 arcsec²), except for those of NGC 6543, for which the Medium Resolution Aperture (MDRS; 4×20 arcsec²) was used. The observations were taken in ‘time-tag’ mode, except those for IC 4593, LSS 1362 and NGC 1360, which were taken in ‘histogram’ mode.

We have reduced the data using the final version of the *FUSE* pipeline, CalFUSE v3.2.2. The ‘CF_edit’ IDL tool (written by Don

Table 2. Utilized data sets.

| Star | Instrument | Res. (Å) | Data ID or source | Date | Aperture (arcsec ²) | λ Range (Å) |
|-----------------|--------------------------|-------------|----------------------|------------|------------------------------------|----------------|
| IC 2448 | <i>FUSE</i> | 0.05 | U1072103 | 2007-06-30 | 30 × 30 | 905–1187 |
| | <i>IUE/High</i> | 0.2 | SWP17473 | 1982-07-23 | 10 × 20 | 1180–1975 |
| | <i>IUE/High</i> | 0.2 | LWR13759 | 1982-07-24 | 10 × 20 | 1975–3125 |
| IC 4593 | <i>FUSE</i> | 0.05 | B0320102 | 2001-08-03 | 30 × 30 | 905–1187 |
| | <i>IUE/High</i> | 0.2 | SWP17948 | 1982-09-13 | 10 × 20 | 1185–1974 |
| | WIYN/Hydra | 0.6 | O. DeMarco | 2002–2003 | | 4050–4730 |
| LSS 1362 | <i>FUSE</i> ¹ | 0.05 | C1770301 | 2002-03-08 | 30 × 30 | 905–1187 |
| | STIS/E140M | 0.05 | O64D02020 | 2001-04-18 | 0.2 × 0.2 | 1177–1709 |
| | <i>IUE/Low</i> | 6 | LWR14242 | 1982-09-24 | 10 × 20 | 1851–3349 |
| NGC 1360 | CTIO/SMARTS | 2.2 | H. Bond | 2003 | | 4020–4940 |
| | <i>FUSE</i> | 0.05 | P1151010 | 2002-07-29 | 30 × 30 | 905–1187 |
| | <i>IUE/High</i> | 0.2 | SWP55902 | 1995-09-10 | 10 × 20 | 1179–1975 |
| | <i>IUE/High</i> | 0.2 | LWP11433 | 1987-08-19 | 10 × 20 | 1975–3348 |
| NGC 1535 | CTIO/SMARTS | 2.2 | H. Bond | 2003 | | 4020–4940 |
| | <i>FUSE</i> | 0.05 | P1150808 | 2001-10-05 | 30 × 30 | 905–1187 |
| | STIS/E140M | 0.05 | O64D04010 | 2001-03-01 | 0.2 × 0.2 | 1180–1700 |
| NGC 2392 | CTIO/SMARTS | 2.2 | H. Bond | 2003 | | 4020–4940 |
| | <i>FUSE</i> | 0.05 | B0320601 | 2001-02-21 | 30 × 30 | 905–1187 |
| | <i>IUE/High</i> | 0.2 | SWP39825 | 1990-10-13 | 10 × 20 | 1187–1975 |
| | <i>IUE/High</i> | 0.2 | LWR15866 | 1983-05-03 | 10 × 20 | 1975–3125 |
| NGC 6058 | CTIO/SMARTS | 2.2 | H. Bond | 2003 | | 4020–4940 |
| | <i>FUSE</i> | 0.05 | B0320401 | 2001-03-26 | 30 × 30 | 905–1187 |
| | <i>IUE/High</i> | 0.2 | SWP38780 | 1990-05-13 | 10 × 20 | 1187–1975 |
| | <i>IUE/Low</i> | 6 | LWR10913 | 1981-06-20 | 10 × 20 | 1975–3349 |
| NGC 6210 | WIYN/Hydra | 0.6 | O. DeMarco | 2002–2003 | | 4050–4730 |
| | <i>FUSE</i> | 0.05 | A0850201 | 2000-08-02 | 30 × 30 | 905–1187 |
| | <i>IUE/High</i> | 0.2 | SWP23133 | 1984-05-29 | 10 × 20 | 1188–1975 |
| NGC 6543 | <i>IUE/High</i> | 0.2 | LWR14149 | 1982-09-11 | 10 × 20 | 1975–3125 |
| | WIYN/Hydra | 0.6 | O. DeMarco | 2002–2003 | | 4050–4730 |
| | <i>FUSE</i> | 0.05 | Q1080200 | 2001-10-01 | 4 × 20 | 905–1187 |
| | STIS/E140H ² | 0.015 | O8O707010 | 2004-07-04 | 0.2 × 0.09 | 1150–1323 |
| | STIS/E140H ² | 0.015 | O8O707020 | 2004-07-04 | 0.2 × 0.09 | 1323–1505 |
| | STIS/E140H ³ | 0.015 | O8O707030 | 2004-07-04 | 0.2 × 0.09 | 1505–1688 |
| | <i>IUE/High</i> | 0.2 | SWP47853 | 1993-06-12 | 10 × 20 | 1688–1950 |
| <i>IUE/High</i> | 0.2 | LWP07710 | 1986-02-23 | 10 × 20 | 1950–3125 | |
| NGC 7662 | INT | 1.5 | O. DeMarco | 1996 | | 3700–6800 |
| | <i>FUSE</i> | 0.05 | B0690301 | 2001-07-20 | 30 × 30 | 905–1187 |
| | <i>IUE/Low</i> | 6 | SWP06467 | 1979-09-10 | 10 × 20 | 1182–1978 |
| | <i>IUE/Low</i> | 6 | LWR03392 | 1979-01-05 | 10 × 20 | 1978–3350 |

¹*FUSE* flux multiplied by 1.05 to match STIS, *IUE* flux levels.

²STIS flux multiplied by 1.1 to match *FUSE*, *IUE* flux levels.

³STIS flux multiplied by 2.05 to match *FUSE*, *IUE* flux levels.

Linder) was used to wavelength register the data from the multiple segments, and to eliminate bad time intervals in the photon-counting stream during the exposure. The pipeline marks some bad time intervals during the exposure (due to bursts, voltage problems, jitter, South Atlantic Anomaly, etc.) but frequently fails to identify periods when the target has drifted outside the aperture. The count rates were examined and regions where the telescope had obviously drifted were marked manually, and then data from all bad time intervals were removed before the spectra were extracted using ‘cf_extract_spectra’. The ‘FUSE_register’ IDL tool was then used to combine the spectral data from all the different segments, after bad regions were eliminated for various reasons (e.g. regions close to the detector edge). An artefact known as the ‘worm’ (caused by a shadow of a component of the instrument falling across the detector) often severely affects the LiF 1B detector, and in these cases the data from that detector were omitted. The worm can also affect the other LiF detectors to a lesser extent, and is less obvious in these

cases, typically manifesting itself as an anomalous minor difference in continuum levels at wavelengths of ~ 1100 – 1150 Å. Despite this, we have used such data as the effect is small and should not affect our analysis. The *FUSE* spectra presented in this paper were constructed by co-adding the ‘good’ regions from the different segments, weighted by their errors, and rebinned to a uniform dispersion of 0.05 Å.

For some stars, continuum flux levels may differ between spectra taken with different telescopes/instruments (or different exposures from the same instrument). Usually these differences are <10 per cent and are most probably due to the positioning of the aperture; however, difficulties in extracting the spectral flux and background in low signal-to-noise ratio (S/N) data may also play a role. In these cases, we have scaled the flux levels of one data set to match the one we were more confident in by multiplying by a constant value, as noted in Table 2.

3 MODELING

3.1 The stellar models

Once its wind has faded and a post-AGB star is on the white dwarf sequence, plane-parallel codes are adequate for modelling its stellar atmosphere. However, for stars with detectable winds, plane-parallel codes become inadequate, as the presence of a wind changes the structure of the atmosphere compared with the hydrostatic case. The atmosphere becomes spherically extended, and density and temperature stratifications are altered. Diagnostic lines may develop an emission component resulting from formation in the stellar wind, and atomic level populations change.

To model the spectra of the central stars, we used CMFGEN (Hillier & Miller 1998, 1999; Hillier et al. 2003; Herald et al. 2005), a line-blanketed non-LTE code suitable for an extended, spherically symmetric expanding atmosphere. The detailed workings of the code are explained in the references above; here we give a brief descriptions of the salient features.

The fundamental photospheric/wind parameters include T_* , R_* , the mass loss rate \dot{M} , the elemental abundances, the velocity law and the wind terminal velocity, v_∞ . R_* is taken to be the inner boundary of the model atmosphere (corresponding to a Rosseland optical depth of ~ 20). The stellar temperature T_* is related to the luminosity and radius by $L = 4\pi R_*^2 \sigma T_*^4$, and the effective temperature (T_{eff}) is similarly defined but at a radius corresponding to a Rosseland optical depth of $2/3$ (R_{eff}). The luminosity is conserved at all depths, so $L = 4\pi R_{\text{eff}}^2 \sigma T_{\text{eff}}^4$.

CMFGEN is a non-hydrodynamic code, so the velocity structure must be specified. We assumed an essentially standard velocity law for the stellar wind $v(r) = v_\infty(1 - r_0/r)^\beta$, where r_0 is roughly equal to R_* . The choice of velocity law mainly affects the profile shape, not the total optical depth of the wind lines, and does not greatly influence the derived stellar parameters. For stars with sufficiently thick winds, such as WR stars and [WR] CSPN, the entire spectrum, including continuum, is formed in the stellar wind. In such cases, a pure wind code is adequate for modelling the observed spectra. However, the stars we examine here have spectra showing absorption lines formed in the photosphere, as well as emission components formed in the stellar wind. The underlying hydrostatic structure is important, and we have used the plane-parallel non-local thermodynamic equilibrium code TLUSTY (Hubeny & Lanz 1995) for its calculation. The wind is connected to the hydrostatic TLUSTY atmosphere (calculated with an effective temperature T_{eff} and gravity $\log g$) using the method described by Hillier et al. (2003). Once a velocity law is specified, the density structure of the wind $\rho(r)$ is then parametrized by the mass-loss rate \dot{M} through the equation of continuity: $\dot{M} = 4\pi R_*^2 \rho(r)v(r)$. However, from fitting the strength of most emission lines in stellar spectra (which originate from ρ^2 processes), one actually can only derive $\dot{M}_{\text{sm}} = (\dot{M}_{\text{cl}}/\sqrt{f})$ from the models, where \dot{M}_{sm} and \dot{M}_{cl} are the smooth- and clumped-wind mass-loss rates, and the degree of clumping is parametrized by the filling factor f . Some diagnostic lines allow f to be constrained, which we discuss more in Section 3.1.1. Unless otherwise noted, \dot{M} refers to \dot{M}_{cl} throughout this paper.

From fitting the model flux levels to the absolute flux levels of the observations, one can derive the ratio of the star's radius to its distance, R_{eff}/D . Only if the distance is firmly known may the stellar radius be well constrained.

It has been found that wind models with the same transformed radius $R_t [\propto R_* (v_\infty / \dot{M})^{2/3}]$ (Schmutz, Hamann & Wessolowski 1989) and v_∞ have the same ionization structure, temperature stratifica-

tion and emerging spectra (aside from appropriate scalings with R_* ; Schmutz et al. 1989; Hamann, Koesterke & Wessolowski 1993). Thus, once the velocity law and abundances are set, one parameter may be fixed (say the radius), and parameter space can then be explored by varying only the other two parameters (e.g. \dot{M} and T_{eff}). For opacities which are proportional to the square of the density, the optical depth of the wind scales as $\propto R_t^{-3}$, so R_t can be thought of as an optical depth parameter. The derived value of R_t is independent of the adopted distance to the star, unlike L , R and \dot{M} . As distances to Galactic CSPN are often unknown or poorly constrained, this is a useful wind parameter for purposes of comparison.

Our sample covers a wide range of temperatures and mass-loss rates and thus does not share a common set of spectral features. Different diagnostics are used in different parameter regimes, which we shall describe on a case by case basis (Section 4). Here we discuss only the more general method of the analysis.

Ideally, one derives the temperature of a star by using diagnostic lines from different ionization stages of the same element, with a more robust determination resulting if the same can be done for multiple elements. Unfortunately, it is often the case in our sample that strong lines are sparse and multiple ionization stages of the same element are not represented (this is especially true for the hotter stars). However, some progress can be made by assuming solar abundances and using lines from different elements to constrain the temperature. This assumption is reasonable for most H-rich CSPN, for which the surface abundances of many elements are not expected to differ significantly from their progenitor's values.

For stars showing strong wind features in their spectra, the terminal wind velocity (v_∞) can be estimated from the blue edge of the saturated P-Cygni absorption features (although H₂ absorption sometimes interferes in the case of far-UV features; see Section 3.2). We generally use all P-Cygni lines to constrain v_∞ , and all wind lines to constrain \dot{M} . We adopted a microturbulence of $\xi_t = 20 \text{ km s}^{-1}$ throughout the wind in the comoving frame model calculation, while a varying microturbulence described by $\xi(r) = \xi_{\text{min}} + (\xi_{\text{max}} - \xi_{\text{min}})v(r)/v_\infty$ was used when calculating the emergent flux. $\xi_{\text{min}} = 10 \text{ km s}^{-1}$ was assumed near the photosphere, while ξ_{max} was taken to be 10 per cent of the terminal velocity. Reasonable changes in this parameter have been found to have little effect on the resulting spectrum (Martins, Schaerer & Hillier 2002; Bouret et al. 2003), with some exceptions for specific lines (also discussed in Keller et al. 2011). We find that with lower values of ξ_{max} , the blue edge of the red component of the O VI profile is often too strong in the synthetic spectrum, although this also depends on \dot{M} , v_∞ and X-rays.

When optical spectra were available, they were used to help constrain $\log g$ values. The wind lines are not particularly sensitive to $\log g$ (Herald & Bianchi 2007), so uncertainty in $\log g$ does not propagate to wind line diagnostics.

3.1.1 Clumping in CSPN winds

The spectra of some stars of our sample show signs of density inhomogeneities or 'clumps'. The concept that clumps will form in the radiation-driven winds of stars has a theoretical basis (Lucy & Solomon 1970; Owocki, Castor & Rybicki 1988; Owocki, Cranmer & Blondin 1994; Gayley & Owocki 1995). It is thought that the line-driven wind flow is inherently unstable which leads to the development of shocks. If these shocks achieve certain temperatures, a super-ionization effect can significantly alter the wind's ionization structure and thus the resulting spectral features. In dense stellar

winds, it is thought that X-ray photons will have little impact on the ionization structure of the bulk ‘cool’ wind (see e.g. the review by Hamann 2010). However, in thin winds (such as those we study here), they may compete better with recombination rates, more dramatically altering the winds ionization structure, and thus have a larger influence in winds of lower mass-loss rates (Macfarlane, Cohen & Wang 1994; Bianchi & Garcia 2002; Garcia & Bianchi 2004; Martins et al. 2005).

Clumping has become a recognized trait of the winds of massive stars, manifesting itself in the form of line profile variability and X-ray emission in observations of WR and O stars. The neglect of clumping has been shown to be the reason that stellar atmosphere models which assumed a smooth wind were unable to simultaneously fit the strength of wind features that vary linearly with the density (such as electron-scattered wings of lines and unsaturated resonance lines) with those that vary as ρ^2 (such as thermal radio emission and the line cores formed via recombination in the stellar wind) (Bianchi, Herald & Garcia 2009).

A proper treatment of clumping by stellar atmosphere codes is currently out of reach because the physical characteristics of the clumps are poorly known (e.g. size, density, shape and velocity), and the computational requirements are very high (e.g. a 3D versus 1D radiative transfer codes are required; see Hillier 2008, for a description of the obstacles). The majority of analyses treating clumping using radiative transfer codes have adopted (as we do here) a simplified *volume-filling-factor* approximation to make the problem tractable. This approach assumes the outflowing medium consists of uniform-density optically thin clumps which are smaller than the mean free path of the photons, with the interclump medium being void. The clumps are parametrized by the volume filling factor f , the physical meaning of which is the ratio of the density of the smooth wind to the clumps ($f = \rho_{\text{smooth}}/\rho_{\text{clump}}$). Deep in the model atmosphere, the wind is smooth up to a specified velocity v_{clump} and then clumping increases outwards with the wind velocity before achieving its terminal value f_{∞} as $f = f_{\infty} + (1 - f_{\infty})\exp(-v/v_{\text{clump}})$. As we discuss later, we found values of $10 \leq v_{\text{clump}} \leq 50 \text{ km s}^{-1}$ to best reproduce line profile characteristics. Elsewhere in this paper, we shall refer to f_{∞} as simply f when discussing clumping.

Using various diagnostics (electron-scattering wings of optical lines, the unsaturated P v $\lambda\lambda 1118, 1128$ resonance line and the subordinate O v $\lambda 1371$ feature) clumping factors have been determined using the treatment described above of $0.05 \leq f \leq 0.25$ for WR stars (Hamann & Koesterke 1998; Herald, Hillier & Schulte-Ladbeck 2001), and $f \lesssim 0.25$ (Repolust, Puls & Herrero 2004; Puls et al. 2006) and $f < 0.1$ for O stars (Bouret et al. 2003; Bouret, Lanz & Hillier 2005; Fullerton, Massa & Prinja 2006; Bianchi, Herald & Garcia 2007). Constraining clumping in the winds of CSPN thus far has proved more difficult, but Todt, Hamann & Gräfener (2008) determined $f < 0.25$ from the electron-scattered wings of optical lines for [WC] stars, and Kudritzki, Urbaneja & Puls (2006) determined $0.02 < f < 1$ for cool ($T_{\text{eff}} \lesssim 37 \text{ kK}$) H-rich CSPN based on comparison of the H α and He II $\lambda 4686$ lines. Prinja et al. (2007) derived $f = 0.08$ for NGC 6543 from the P v feature. In the case of H-deficient CSPN, Grosdidier, Moffat & Acker (2003) presented observational evidence that suggests winds of some [WC] and [WO] type CSPN are clumped.

As clumping seems to be prevalent in radiatively driven winds, but clumping factors in CSPN winds are not well established, we initially assumed a clumping factor of $f = 0.1$. However, in the course of our analysis it became clear that some stars required higher degrees of clumping, which we discuss in Section 5.

3.1.2 X-rays in CSPN winds

As mentioned previously (Section 3.1.1), a by-product of a shocked wind is X-rays, and this mechanism has been proposed to explain the observed X-ray emission from massive O and B stars. The only viable explanation for the relatively strong observed O v i profiles seen in the spectra of many (relatively cool) O and B stars is Auger ionization from O iv (Cassinelli & Olson 1979), which requires X-rays to occur (see e.g. Zsargó et al. 2008, for a discussion). It has been demonstrated that X-rays are needed to reproduce the strong O v i $\lambda\lambda 1032, 38$ line seen in the far-UV spectra of some O stars (Bianchi & Garcia 2002; Garcia & Bianchi 2004; Martins et al. 2005), illustrating the possible utility of this line (and lines of other ‘super-ions’ which may be influenced by X-rays such as N v $\lambda\lambda 1239, 1242$ and S v i $\lambda\lambda 933, 944$) as indirect X-ray diagnostics. In very hot CSPN (i.e. $T_{\text{eff}} \gtrsim 80 \text{ kK}$), the ionization of the wind is high enough that this line can be reproduced without the inclusion of X-rays (e.g. Herald & Bianchi 2004a) in the model atmospheres. However, we have found examples of CSPN in the Large Magellanic Cloud for which the other stellar diagnostics implied a relatively cool star (i.e. $T_{\text{eff}} \sim 50 \text{ kK}$), but with a strong O v i spectral feature that could only be simultaneously fitted with the other features by including X-rays in the wind (Herald & Bianchi 2007).

Since stellar parameter determinations depend on the ionization structure of the wind, it is crucial to understand the influence of X-rays in stellar winds in general. The O v i $\lambda\lambda 1032, 1038$ resonance lines are present in the spectra of all our sample CSPN. For some stars of our sample, our models failed to achieve the observed strength of the O v i lines simultaneously with the other, lower ionization diagnostics. In these cases, we calculated additional models which allow for the presence of X-rays, presumably from shocks, in the wind. CMFGEN implements X-rays as described in Martins et al. (2005). In summary, shock sources are assumed to be distributed throughout the atmosphere once the wind achieves a certain velocity, with emissivities taken from Raymond & Smith (1977). The shock parameters include the shock temperature T_x (which controls the energy distribution of the shocks), the X-ray volume filling factor f_x (which sets the level of emission) and the velocity of the wind where the shocks begin v_x . Work on X-rays in the winds of massive stars indicates the onset of shocks begin at a radius of $r \simeq 1.5 R_*$ (Leutenegger et al. 2006; Owocki & Cohen 2006; Cohen et al. 2010). Following this, and in consideration of some of our clumping results we discuss more in Section 5.1, we have adopted $v_x \sim 50 \text{ km s}^{-1}$, which roughly corresponds to this radius for most of our stars. In practice, our analysis shows v_x has little effect as long as f_x is adjusted to preserve L_x , the X-ray luminosity. For our basic X-ray model, we assumed two shock components of temperatures 300 and 500 kK, typical of high-energy photons in O-type stars (e.g. Cohen et al. 2003; Schulz et al. 2003), and adjusted the volume filling factor until adequate fits of the O v i feature were achieved. CMFGEN reports the total X-ray luminosity injected into the wind, as well as what would be observed (the X-ray flux which escapes). When referring to these model X-ray fluxes elsewhere in this paper, we will be referring to the latter unless otherwise stated (as this is what can actually be measured).

3.1.3 Abundances and model ions

Throughout this work, the values for solar abundances of the elements are adopted from Asplund, Grevesse & Sauval (2005), the nomenclature X_i represents the mass fraction of element i and ‘ X_{\odot} ’ denotes the solar value.

Table 3. Ion superlevels/levels.

| Element | I | II | III | IV | V | VI | VII | VIII | IX | X |
|---------|--------|--------|----------|---------|---------|---------|----------|-----------|----------|---------|
| H | 20, 30 | | | | | | | | | |
| He | 40, 45 | 22, 30 | | | | | | | | |
| C | | | 30, 54 | 13, 18 | | | | | | |
| N | | | 34, 70 | 29, 53 | 13, 21 | | | | | |
| O | | | 25, 45 | 29, 48 | 41, 78 | 13, 19 | | | | |
| Ne | | 14, 48 | 40, 182 | 45, 355 | 37, 166 | 36, 202 | 38, 182 | 24, 47 | | |
| Na | | | 16, 229 | 41, 240 | 31, 143 | 52, 452 | 37, 251 | | | |
| Mg | | | 17, 201 | 27, 264 | 43, 311 | 46, 444 | 54, 476 | | | |
| Al | | | 21, 65 | 62, 201 | 29, 95 | 20, 73 | 21, 41 | | | |
| Si | | | | 22, 33 | 33, 98 | 33, 71 | | | | |
| P | | | | 36, 178 | 16, 62 | | | | | |
| S | | | | 51, 142 | 31, 98 | 28, 58 | | | | |
| Cl | | | | 40, 129 | 26, 80 | 18, 44 | 17, 28 | | | |
| Ar | | | 10, 36 | 31, 105 | 38, 99 | 30, 205 | 33, 174 | 57, 72 | | |
| K | | | 20, 40 | 40, 611 | 36, 305 | 54, 513 | | | | |
| Ca | | | 37, 142 | 31, 137 | 43, 107 | 40, 127 | 55, 514 | 54, 445 | 35, 367 | 31, 79 |
| Cr | | | | 29, 234 | 30, 223 | 30, 215 | | | | |
| Co | | | | 40, 343 | 30, 367 | 26, 224 | 45, 1000 | 50, 1217 | 24, 355 | |
| Ni | | | 47, 1000 | 36, 200 | 46, 183 | 37, 314 | 61, 1000 | 113, 1000 | 75, 1217 | |
| Mn | | | | 39, 464 | 16, 80 | 23, 181 | 20, 203 | | | |
| Fe | | | | 51, 294 | 47, 191 | 44, 433 | 41, 252 | 53, 324 | 52, 490 | 43, 210 |

Even using modern computers, running stellar atmosphere codes which account for line-blanketing elements can be computationally demanding. To make the calculations tractable, CMFGEN utilizes the concept of ‘superlevels’ for the model ions, whereby levels of similar energies are grouped together and treated as a single level in the rate equations (after Anderson 1989). Using this approach, the following ions were included in the model atmospheres used to constrain the stellar parameters: H, He I–He II, C III–C IV, N III–N V, O III–O VI, Ne III–Ne VIII, Si IV, P IV–P V, S IV–S VI, Fe IV–Fe X. Some ionization stages may be omitted from the calculations in the interest of time and/or easing convergence, if they are unimportant (essentially unpopulated). For example, low ionization stages in very hot stars and vice versa. Once parameters were established using diagnostic lines from these elements, additional elements were included in the models, usually one at a time, to determine if they offered any useful diagnostics over the large parameter range spanned by our sample, and to confirm that their impact was minor enough that they could be safely neglected when determining the stellar parameters (other than their abundances). These additional ions/elements include Ar III–Ar VIII, Na III–Na VII, Mg III–Mg VII, Al III–Al VII, Cl IV–Cl VII, K III–K VI, Ca III–Ca X, Cr VI–Cr VII, Mn IV–Mn VII, Co IV–Co IX and Ni III–Ni IX. The results of these tests are discussed in Section 5.3. Ions and the number of levels and superlevels included in the model calculations are given in Table 3.

3.2 Corrections for molecular and atomic hydrogen, reddening

In this paper, when comparing with flux-calibrated spectra, we have applied the effects of reddening to the model spectra using the Cardelli, Clayton & Mathis (1989, hereafter CCM) Galactic reddening law (assuming $R_v = 3.1$), extrapolated down to far-UV wavelengths. This approach is justified as Gordon, Cartledge & Clayton (2009) found little deviation from the CCM reddening law in their *FUSE*-based study of extinction curves.

Absorption due to atomic (H I) and molecular hydrogen (H₂) along the sightline can greatly complicate the far-UV spectra of

Table 4. Interstellar/circumstellar parameters.

| Star | logN(H I) | logN(H ₂) | T(gas) (K) | E_{B-V} (mag) |
|-----------------------|-----------|-----------------------|---------------|--------------------|
| IC 2448 | 21.0 | 16.0 | 80 | 0.055 |
| IC 4593 | 20.8 | 19.3 | 80 | 0.060 |
| LSS 1362 | 21.0 | 20.3 | 80 | 0.105 |
| NGC 1360 | 19.9 | 14.3 | 80 | 0.005 |
| NGC 1535 ¹ | 20.8 | 18.7 | 80 | 0.055 |
| | – | 16.4 | 400 | |
| NGC 2392 | 20.8 | 18.0 | 80 | 0.070 |
| | – | 18.0 | 200 | |
| NGC 6058 | 20.3 | 16.0 | 80 | 0.005 |
| NGC 6210 | 20.7 | 19.7 | 80 | 0.100 |
| NGC 6543 | 20.7 | 16.3 | 80 | 0.035 |
| | – | 16.0 | 1500 | |
| NGC 7662 | 21.0 | 20.0 | 80 | 0.080 |

¹Parameters for NGC 1535 from Herald & Bianchi (2004a).

these objects. H₂ transitions from the Lyman and Werner series blanket the *FUSE* range, particularly at shorter wavelengths (i.e. <1100 Å). These absorption effects are treated as described in Herald & Bianchi (2002, 2004a,b). We do not attempt a rigorous determination of the column densities here. Rather, our goal was to determine the hydrogen absorption parameters adequately enough to be able to separate the stellar features from the interstellar absorptions. The parameters of the hydrogen absorption models used are given in Table 4, along with our utilized E_{B-V} values, determined by fitting the far-UV and UV spectra. In some cases (NGC 1535, 2392 and 6543), the addition of a second component of hot molecular hydrogen (presumably circumstellar, rather than interstellar) better matches observations, as has been found for other CSPN (Herald & Bianchi 2004a,b, 2007; McCandliss et al. 2007). We estimate the uncertainty in our H I column densities to be ± 0.1 (log) and those of our E_{B-V} determinations to be ± 0.02 mag (although it is higher in the cases of NGC 7662 and 2448, due to low-resolution UV spectra and nebular contamination, respectively).

4 RESULTS FOR INDIVIDUAL STARS

In this section, we discuss the diagnostics used and stellar and wind parameters derived for our 10 sample stars on an individual basis. We defer some topics that apply to the sample overall until the next section, particularly, clumping, X-rays, the circumstellar

environment and results concerning our testing of various trace elements in the model atmospheres.

Our best-fitting models are shown along with the observations in Figs 1–6. The model spectra, both with and without the effects of our atomic and molecular hydrogen absorption models applied (Section 3.2), are shown, and from Figs 1, 2 and 7 one can see the

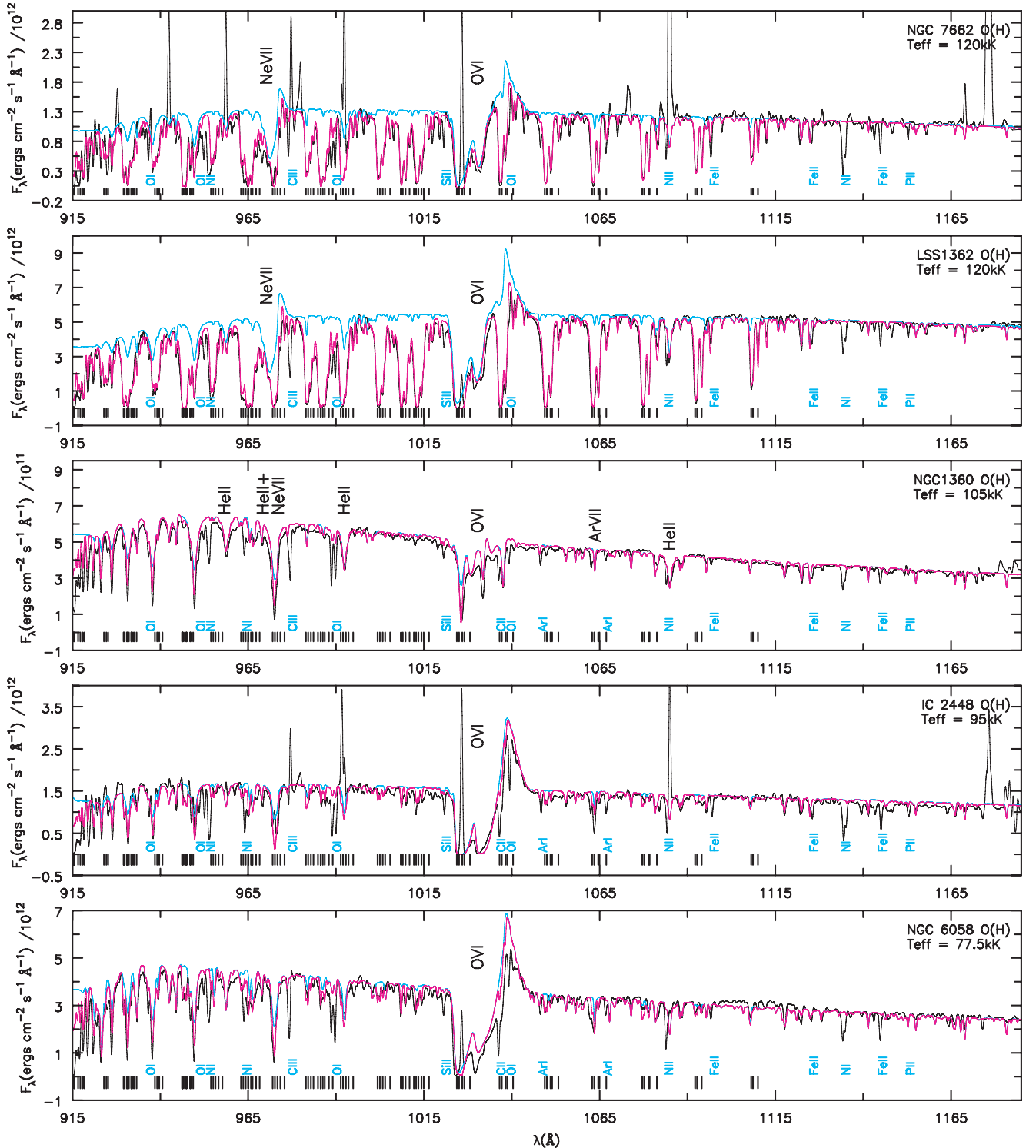


Figure 1. Far-UV observations (black) and our best-fitting models with/without (pink/aqua) H1 and H2 absorption effects applied for the hotter sample stars (black tick marks denote where the stronger H2 transitions occur). The stronger stellar features are labelled, as are IS absorption features. Narrow emission features are airglow and nebular lines. The spectra have been convolved to a resolution of 0.5 \AA for clarity.

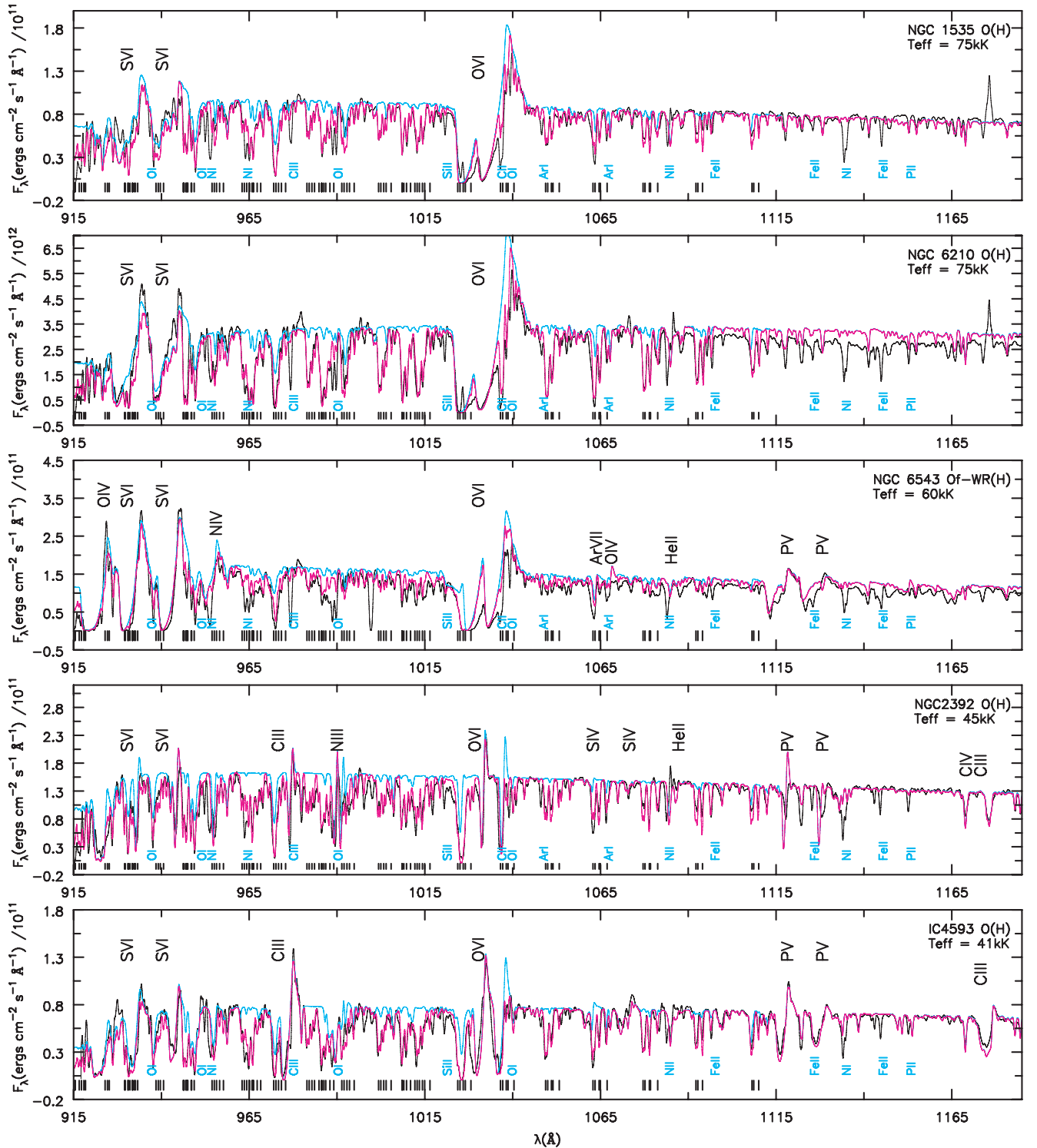


Figure 2. Same as Fig. 1, for the cooler central stars.

necessity of modelling these effects in identifying the underlying spectral component of the *FUSE* spectra.

Our derived central star parameters are summarized in Table 5. Columns 2–8 give the stellar parameters derived by fitting the spectral line diagnostics with *CMFGEN*. Parameters that can be derived independent of knowledge of the star’s distance are listed first, which include the gravity, stellar and effective temperatures, the

wind terminal velocity, clumping factors, transformed radius and the ratio of the X-ray luminosity to the stellar luminosity (discussed more in Section 5.2). By scaling the best-fitting model, reddened with the E_{B-V} values given in Table 4, to the observed flux, we also derive R_{eff}/D (column 9). In columns 10–15, we give two sets of additional parameters. The first set (shown at the top of the table) is derived appropriately for an effective radius corresponding to an

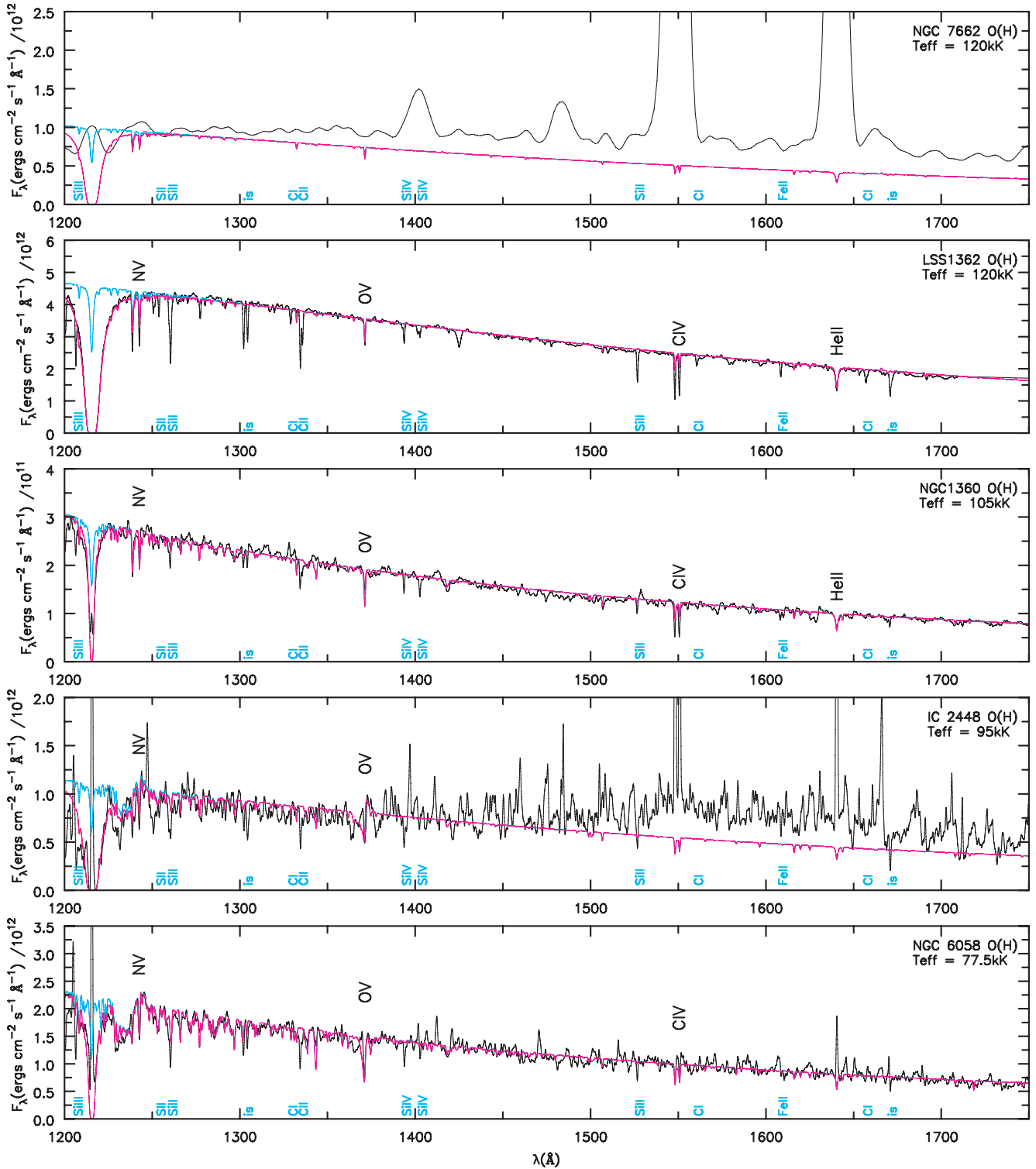


Figure 3. UV observations (black) and our best-fitting models with/without (pink/aqua) H I absorption effects applied for the hotter sample stars. The stronger stellar features are labelled. Depending on the nebular diameter and the aperture size used to acquire the spectra, some nebular lines may be present, and the nebular continuum may add to flux levels $\gtrsim 1300$ Å (as appears to be the case for NGC 7662 and IC 2448). The spectra have been convolved to a resolution of 0.75 Å for clarity.

assumed stellar mass of $M = 0.6 M_{\odot}$, thought to be the typical value for the final mass of a CSPN (which results in a derived spectroscopic distance). To illustrate the effect of the uncertainty in the stellar mass on the derived parameters, note that adopting a mass of

$M = 0.5/0.8 M_{\odot}$, representing the predicted lower/upper final mass values from evolutionary theory, alters presented table values of the radius (and distance) by -10 per cent/ $+15$ per cent, and, roughly, the luminosity by -17 per cent/ $+35$ per cent and the mass-loss

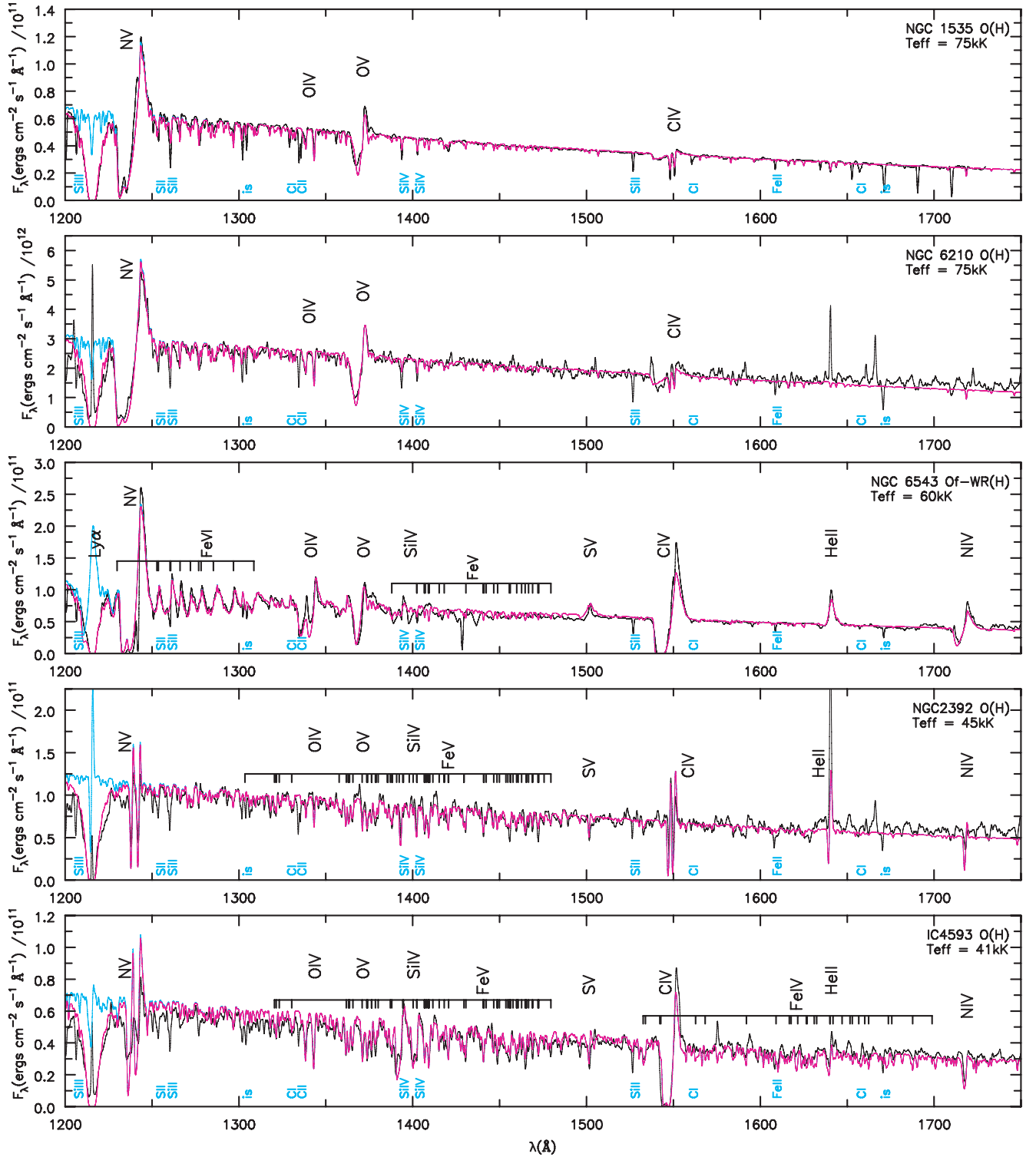


Figure 4. Same as Fig. 3, for the cooler central stars.

rate by -13 per cent/ $+25$ per cent. The second set of parameters (shown at the bottom of the table) is found by adopting the literature distances listed in Table 1 and deriving R_{eff} from R_{eff}/D , and the other parameters consequently. The three stars without distance determinations (LSS 1362, NGC 6058 and IC 4593) are only listed in the first set. Uncertainties in T_{eff} are discussed in the sections on individual stars. We do not include uncertainties on R_1 or \dot{M} , as

these are dominated by those in the clumping filling factor f . For example, constraining f to $0.01 < f < 0.1$ implies a factor of three uncertainty in \dot{M} , while we can typically constrain \dot{M} to within a factor of 2 for a specific value of f . The derived parameters are discussed more in Section 5.4.

In the following subsections, we discuss the modelling diagnostics and results for each of the individual CSPN, roughly in order of

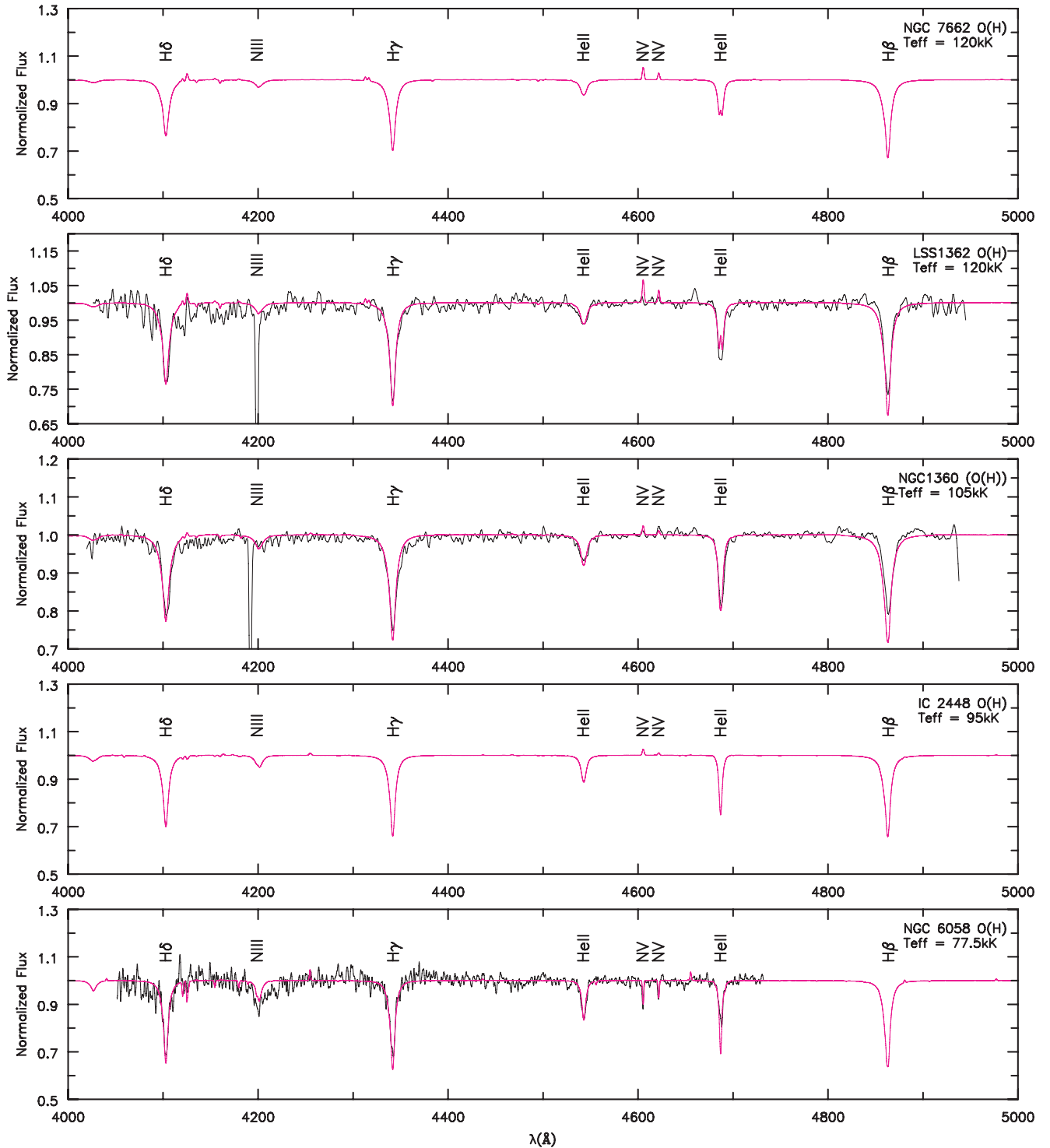


Figure 5. Optical blue spectra (black) and our best-fitting models (pink) for the hotter sample stars. The stronger stellar features are labelled, and the model spectra are convolved to the spectral resolution of the data in each case (for IC 2448 and NGC 7662, we lack optical spectra and only show the models).

decreasing stellar temperature. Many spectral features are common in multiple stars of the sample, and are the strongest representatives of their ionization stages present in the far-UV/UV spectra. These include S VI $\lambda\lambda 933.4, 944.5$, Ne VII $\lambda 973.3$, C III $\lambda 977.0$, O VI $\lambda\lambda 1031.9, 1037.6$, P V $\lambda\lambda 1118.0, 1128.0$, N V $\lambda\lambda 1238.8, 1242.8$, O IV $\lambda\lambda 1338.6, 1343.0, 1343.5$, O V $\lambda 1371.3$, Si IV $\lambda\lambda 1393.7, 1402.8$, C IV $\lambda\lambda 1548.2, 1550.8$, He II $\lambda 1640.4$ and N IV $\lambda 1718.5$. For shorthand

in the discussion that follows, we will omit the wavelength when referring to these lines (e.g. ‘the C IV doublet’ is C IV $\lambda\lambda 1548, 1551$, and ‘the O V feature’ would refer to O V $\lambda 1371$). We will include the wavelength when referring to other lines of these elements.

Likewise, there are several stars which show multitudes of (relatively) weak absorption lines from various ionization stages of iron. These ‘forests’ tend to appear at shorter wavelengths the

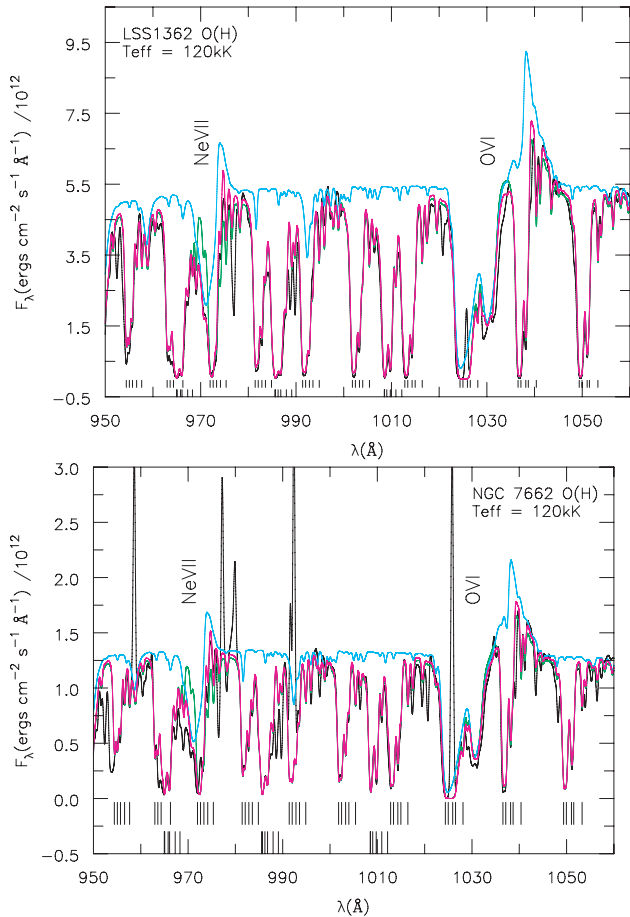


Figure 7. LSS 1362 (top) and NGC 7662 (bottom). *FUSE* observations of the Ne VII $\lambda 973$ and O VI $\lambda\lambda 1032, 1038$ profiles (black), along with our models with (pink) and without (aqua) the effects of interstellar absorption from H I and H₂ applied. We also show the same models (with IS absorption effects applied), but without neon in the model atmosphere calculations (green). One can see deviations from the observations in the 970–980 Å range when neon is omitted. This figure also illustrates the necessity of accounting for interstellar H₂ in modelling the underlying stellar spectrum.

$\lambda 1455.6$, $\lambda 1456.2$, $\lambda 1459.8$, $\lambda 1462.6$, $\lambda 1464.7$, $\lambda 1466.6$, $\lambda 1469.0$, $\lambda 1472.1$, $\lambda 1479.5$.

4.1 The Ne VII signatures of LSS 1362 and NGC 7662

We group NGC 7662 with LSS 1362, as their *FUSE* spectra are very similar (although that of the former is contaminated by numerous airglow and nebular emission lines). The only observed wind features for both these stars are seen in their *FUSE* spectra, from Ne VII and O VI. The neon feature is not immediately obvious in either case, as it is masked by H₂ absorption, but its presence can be inferred from its P-Cygni absorption trough (Fig. 7). Under the assumption of solar abundances, these two features constrain temperatures for both stars to ~ 110 – 125 kK (in hotter models, Ne VII is too strong while O VI is too weak, while for cooler models the reverse is true). These features, being unsaturated, are sensitive to M (Bianchi & Herald 2007; Herald & Bianchi 2009) and were used to constrain this parameter (we have adopted $f = 0.1$ as discussed in Section 3.1.1). The Ne VII line can appear as a strong P-Cygni profile in H-deficient CSPN, where the neon surface abundance is thought to reach 10 times the solar value (Herald et al. 2005).

The high-resolution STIS data of LSS 1362 (from 1200 to 1700 Å) show many strong photospheric absorption lines, including the N v, O v and C IV lines. The O v line is well fitted in our models, as are the O VI $\lambda\lambda 1022, 1025$ and C IV $\lambda 1169$ absorption features. The N v and C IV features appear to be weak in Fig. 3; however, when viewed at full resolution, the observed profiles are seen as superpositions of stellar and circumstellar components, with the latter blueshifted with respect to the photospheric absorption line (Fig. 8). We discuss this more in Section 5.5.

Comparison with the optical hydrogen Balmer and He II spectrum implies $\log g = 5.7 \pm 0.3$ for LSS 1362. Our analysis resulted in a somewhat higher temperature and gravity than was found in earlier (optical- and UV-based) analyses ($T_{\text{eff}} \simeq 100$ kK, $\log g = 5.3$; Schonberner & Drilling 1984; Heber, Werner & Drilling 1988).

The only UV data available for NGC 7662 are low-resolution (~ 6 Å) *IUE* spectra and are not useful in constraining stellar parameters (they appear to show nebular emission features). We have therefore assumed $\log g = 5.7$ (based on the similarity of this star's *FUSE* spectrum to that of LSS 1362). Our derived temperature is consistent with NGC 7662 being a high-excitation PN, as has been noted by many authors (e.g. Lamé & Pogge 1996; Hyung & Aller 1997). Nebular diagnostics suggest CS temperatures of $T_{\text{eff}} > 100$ kK (Hyung & Aller 1997). Although the nebular structure of NGC 7662 has been studied extensively (Pottasch et al. 2001; Guerrero, Jaxon & Chu 2004; Perinotto et al. 2004), we are not aware of prior determinations of its temperature through spectral modelling.

4.2 The fading wind of NGC 1360

The *FUSE* and *IUE* high-resolution spectra of this star show mainly an absorption line spectrum. Models with $95 \leq T_{\text{eff}} \leq 115$ kK adequately fit the observed absorption lines, which include the N v and O v lines, C IV $\lambda 1169$, as well as the Fe VII absorption features. The lack of a significant Fe VI absorptions helps put a lower limit on the temperature, while the absence of a significant Ne VII feature helps define our upper limit. The UV C IV doublet is stronger in the observations, but close inspection reveals this is most probably due to a nebular component (as for LSS 1362, see Section 4.1 and Fig. 8), as the observed absorption lines are blueshifted by an amount which corresponds to the nebular expansion velocity of $v_{\text{exp}} \simeq 26$ km s⁻¹ as measured by García-Díaz et al. (2008) (unlike the other UV absorption features such as N v and O v, which display no such shift after the regression velocity has been removed). We derive $\log g = 5.7_{-0.2}^{+0.3}$ based on both the hydrogen Lyman and helium features in the *FUSE* range (915–960 Å) and the hydrogen Balmer and helium lines in the optical range.

Our CS temperature of $T_{\text{eff}} \simeq 105$ kK is similar to those derived from previous analyses [$T_{\text{eff}} = 97$ kK, $\log g = 5.3$ (Traulsen et al. 2005) from *FUSE* and *HST* data; $T_{\text{eff}} = 110$ kK, $\log g = 5.6$ (Hoare et al. 1996) from *Extreme Ultraviolet Explorer* data]. Earlier studies of this star have found no signs of a detectable stellar wind (e.g. Jordan, Werner & O'Toole 2005; Guerrero, Ramos-Larios & Massa 2010). However, close inspection of the O VI doublet profile in the *FUSE* spectra does indicate the presence of a stellar wind, albeit a weak one (see Fig. 9). The dips seen at $\lambda 1029$ and $\lambda 1034$ are best explained as P-Cygni absorption components, with the slight rise in flux at $\lambda 1040$ as being a weak P-Cygni emission component. This star is thus an important example of a CSPN with a wind at the threshold of detectability, and we have invested some time in analysing this profile further. As mentioned previously, we have adopted a $\beta = 1$ velocity law in the analysis of our sample. However, using this velocity structure in the case of NGC 1360 results

Table 5. Derived stellar parameters.¹

| Star | $\log g$ | T^* (kK) | T_{eff} (kK) | v_{∞} (km s ⁻¹) | $\log R_t$ (R _⊙) | f | $\log L_x^2$ (L [*]) | R_{eff}/D (R _⊙ kpc ⁻¹) | R_{eff} (R _⊙) | M (M _⊙) | D (kpc) | $\log L$ (L _⊙) | $\log \dot{M}_{\text{cl}}$ (M _⊙ yr ⁻¹) |
|--|-------------------------------------|---------------|--------------------------|---------------------------------------|---------------------------------|-------------|-----------------------------------|---|---------------------------------------|--------------------------|--------------|-------------------------------|--|
| Parameters assuming $M = 0.6 M_{\odot}$ | | | | | | | | | | | | | |
| NGC 7662 | 5.7 | 121.8 | 119.4 | 2250 | 2.02 | <i>0.10</i> | -2.0/NA | 0.078 | 0.181 | <i>0.60</i> | 2.32 | 3.78 | -8.72 |
| LSS 1362 | 5.7 ± 0.3 | 121.8 | 119.4 | 2400 | 2.02 | <i>0.10</i> | -2.0/NA | 0.190 | 0.181 | <i>0.60</i> | 0.95 | 3.78 | -8.70 |
| NGC 1360 ³ | 5.7 ^{+0.3} _{-0.2} | 106.0 | 104.5 | 1250 | 3.11 | <i>0.10</i> | -3.7/NA | 0.321 | 0.181 | <i>0.60</i> | 0.56 | 3.55 | -10.60 |
| IC 2448 | 5.4 ^{+0.3} _{-0.4} | 98.5 | 95.0 | 2000 | 2.02 | <i>0.10</i> | -4.4/NA | 0.089 | 0.256 | <i>0.60</i> | 2.86 | 3.68 | -8.57 |
| NGC 6058 | 4.8 ± 0.3 | 91.5 | 77.1 | 2300 | 2.41 | 0.04 | -6.2/-4.7 | 0.118 | 0.510 | <i>0.60</i> | 4.31 | 3.92 | -9.02 |
| NGC 1535 | 4.8 ± 0.3 | 85.0 | 74.4 | 2000 | 2.01 | 0.10 | -6.2/-4.9 | 0.261 | 0.510 | <i>0.60</i> | 1.96 | 3.86 | -8.22 |
| NGC 6210 | 4.8 ± 0.2 | 88.3 | 75.0 | 2150 | 1.88 | 0.10 | -6.1/-4.8 | 0.230 | 0.510 | <i>0.60</i> | 2.22 | 3.87 | -8.04 |
| NGC 6543 | 4.7 ± 0.3 | 60.4 | 59.7 | 1500 | 1.43 | 0.04 | -9.7/-5.5 | 0.367 | 0.573 | <i>0.60</i> | 1.56 | 3.57 | -7.45 |
| NGC 2392 | 4.0 ± 0.2 | 47.9 | 45.0 | 300 | 1.59 | <i>0.10</i> | -16.9/-4.4 | 0.583 | 1.282 | <i>0.60</i> | 2.20 | 3.78 | -7.72 |
| IC 4593 | 3.7 ± 0.2 | 48.1 | 41.0 | 750 | 1.88 | 0.04 | -19.8/-4.8 | 0.526 | 1.811 | <i>0.60</i> | 3.44 | 3.92 | -7.87 |
| Parameters assuming distances from Table 1 | | | | | | | | | | | | | |
| NGC 7662 | | | | | | | | | 0.062 | 0.07 | <i>0.80</i> | 2.85 | -9.42 |
| NGC 1360 ³ | | | | | | | | | 0.112 | 0.23 | <i>0.35</i> | 3.13 | -10.91 |
| IC 2448 | | | | | | | | | 0.123 | 0.14 | <i>1.38</i> | 3.05 | -9.04 |
| NGC 1535 | | | | | | | | | 0.602 | 0.84 | <i>2.31</i> | 4.00 | -8.11 |
| NGC 6210 | | | | | | | | | 0.361 | 0.30 | <i>1.57</i> | 3.57 | -8.27 |
| NGC 6543 | | | | | | | | | 0.367 | 0.25 | <i>1.00</i> | 3.19 | -7.74 |
| NGC 2392 | | | | | | | | | 0.933 | 0.32 | <i>1.60</i> | 3.51 | -7.93 |

¹ *Italics* denote adopted values, rather than derived by modelling.

² X-ray luminosity > 0.1 keV, for models without and with X-rays from shocks included in the model winds.

³ Model for NGC 1360 used velocity law with $\beta = 1.5$, for all others $\beta = 1$ was used.

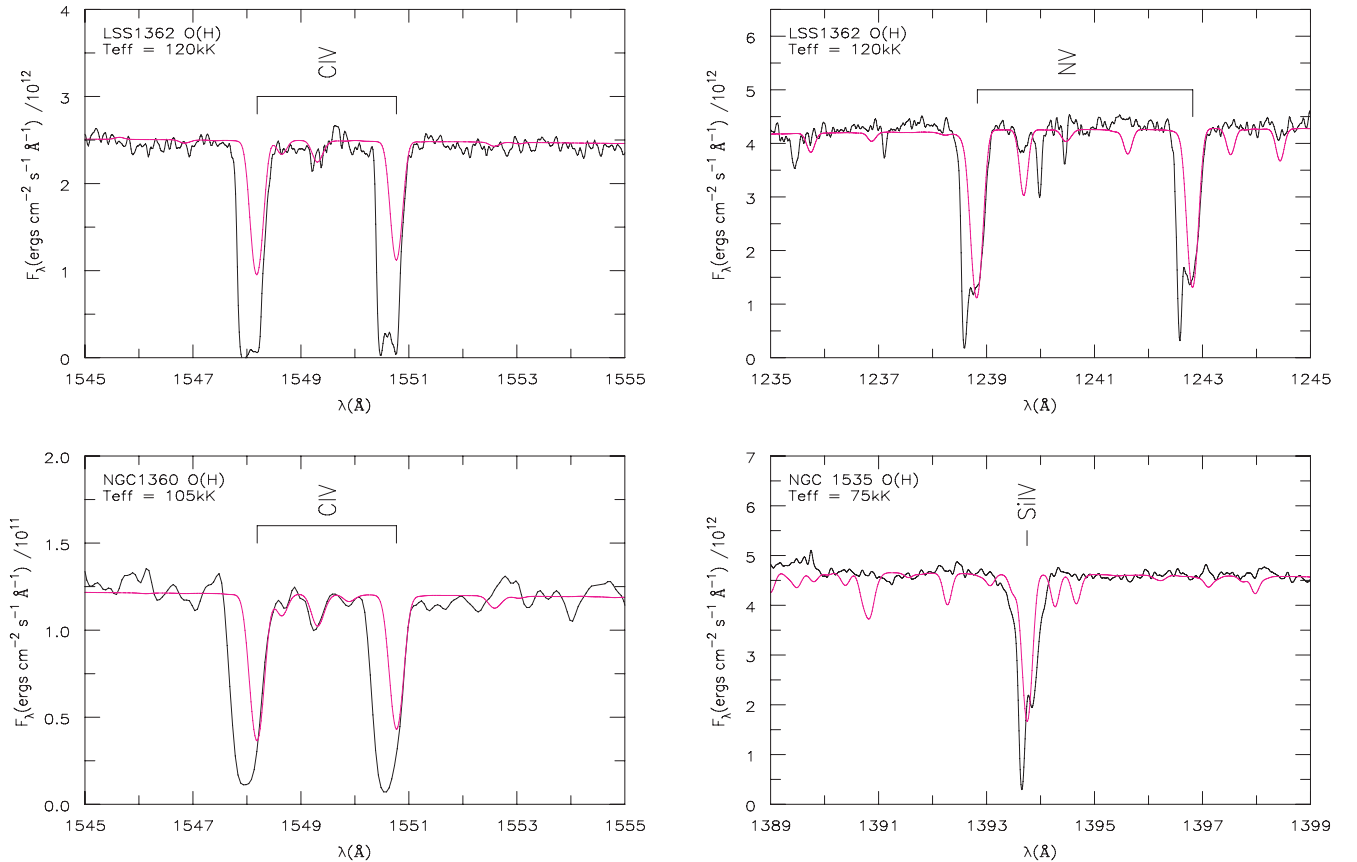


Figure 8. Circumstellar absorption. Observations (black), and models (pink) of the LSS 1362 C iv (top left) and N v (top right) doublets, the NGC 1360 C iv doublet (bottom left) and the NGC 1535 Si iv $\lambda 1393.7$ line (bottom right). The LSS 1362 and NGC 1535 spectra are STIS E140M ($\delta V = 6.5$ km s⁻¹) data, which allow the two-component nature of the profiles to be discerned. The lines appear to be a stellar absorption component blended with one from circumstellar material. The lower resolution of the NGC 1360 *IUE* spectrum (~ 0.2 Å) makes the situation ambiguous, but the velocity shift of the observed profiles suggests that they may be due to circumstellar material or to outflow not reproduced by the model.

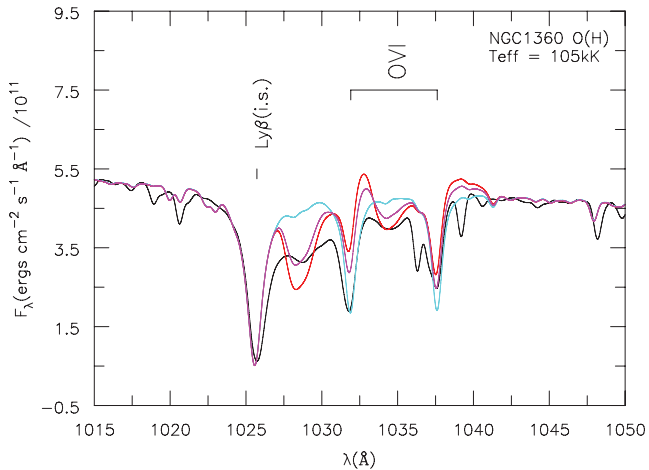


Figure 9. NGC 1360. *FUSE* observations of the OVI $\lambda\lambda 1032, 1038$ profile (black), along with models ($\beta = 1.5$) of varying \dot{M} : 1.0×10^{-11} (aqua), 2.5×10^{-11} (pink), and $3.16 \times 10^{-11} M_{\odot} \text{ yr}^{-1}$ (red). The profile is not reproducible without a stellar wind of $\dot{M} \gtrsim 2.2 \times 10^{-11} M_{\odot} \text{ yr}^{-1}$ (clumped, $\gtrsim 7 \times 10^{-11} M_{\odot} \text{ yr}^{-1}$ smooth). Only this line profile reveals the presence of a stellar wind for this object, illustrating the importance of the far-UV wavelength range in studying post-AGB objects with fading winds. Note the strong absorption feature at $\sim 1025.7 \text{ \AA}$ is a combination of the photospheric Ly β line combined with interstellar absorption. The quoted mass-loss rates correspond to an assumed $M = 0.6 M_{\odot}$ (see Section 4).

in P-Cygni absorption troughs which are too sharply peaked. We achieved the best match of the shape of the overall profile using $\beta = 1.5$ (higher values resulted in too flat an absorption profile). The blending of the O VI profile with the strong Ly β $\lambda 1026$ feature (itself a combination of photospheric and interstellar absorption) results in a fair degree of uncertainty in location of the blue edge of the O VI absorption components. However, we find that models with $1500 \leq v_{\infty} \leq 1200 \text{ km s}^{-1}$ produce reasonable fits. Our model still has trouble with the blue edge of the absorption trough, which rises too steeply. However, the overall shape and strength of the profile are adequately reproduced. We have performed similar fits using models at the lower and upper limits of temperature for this star (95 and 115 kK) and constrain the mass-loss rate to be $4.0 \times 10^{-12} \lesssim \dot{M} \lesssim 1.0 \times 10^{-10} M_{\odot} \text{ yr}^{-1}$ using the assumed clumping factor of $f = 0.1$ (see Section 3.1.1) and assuming $M = 0.6 M_{\odot}$ (Section 4). Removing the assumption of a clumped wind yields limits about three times higher, placing an upper limit of $\dot{M} \lesssim 3 \times 10^{-10} M_{\odot} \text{ yr}^{-1}$, the smallest determined value for a CSPN to the knowledge of these authors.

The nebula of NGC 1360 differs from the usual PN morphologies (ring, bipolar, etc), appearing as a thick shell with no sharp inner edge. Goldman et al. (2004) interpreted this structure as indicating a lack of compression of the nebula due to a stellar fast wind. García-Díaz et al. (2008) proposed this morphology may come to exist after the stellar wind becomes negligible, at which point the hot shocked bubble loses pressure and the thermal pressure of the photoionized region of the swept-up shell becomes dominant, causing the material of the inner shell to expand back towards the central star, filling the cavity with ionized gas. Our derived wind parameters may help place constraints on when exactly this phase occurs.

We also remark that NGC 1360 was classified by Mendez & Niemelä (1977) as a spectroscopic binary with a period of about 8 days. However, this was not confirmed in the detailed radial velocity study of Wehmeyer & Kohoutek (1979), and other subsequent investigations have failed to detect a companion. NGC 1360 is no-

table because it is one of the few CSPN (along with LSS 1362) for which a strong magnetic field has been detected (on the order of kG; Jordan et al. 2005).

4.3 IC 2448

The only wind features seen in the available spectra of IC 2488 are from O VI in the *FUSE* range, and N V and O V in the (noisy) high-resolution *IUE* spectra. These features are well fitted by our model ($T_{\text{eff}} = 95 \text{ kK}$, $R_t = 1.8$), as are the photospheric absorption lines from O VI $\lambda\lambda 1122.4, 1124.9$, C IV $\lambda 1169$ and the Fe VII spectrum. In hotter models, the unobserved Ne VII feature appears (assuming a solar neon abundance). We lack optical spectra for this object, and we are only able to loosely constrain the gravity based on the far-UV Lyman spectrum to be $\log g = 5.4^{+0.3}_{-0.4}$.

The *IUE* spectrum shows many nebular emission lines, as well as a significant nebular continuum component for $\lambda \gtrsim 1300 \text{ \AA}$. The nebular contamination is more prominent in this case because the small nebula (9 arcsec, see Table 1) is contained entirely in the *IUE* aperture.

4.4 NGC 6058

Models with $75 \leq T_{\text{eff}} \leq 80 \text{ kK}$ and $R_t \simeq 2.5 R_{\odot}$ well fit the observed wind features of NGC 6058: O VI and N V, while also adequately fitting the photospheric absorption lines in both the *FUSE* and high-resolution *IUE* spectra: P V, C IV, C IV $\lambda 1169$ and the Fe VI/Fe VII spectrum. The O IV absorption feature is a bit strong in the $T_{\text{eff}} = 75 \text{ kK}$ models while the O VI line is slightly weak, while for the $T_{\text{eff}} = 80 \text{ kK}$ they are well fitted but N V appears a bit weak. The (shown) $T_{\text{eff}} = 77.5 \text{ kK}$ model fits these features adequately although the O VI absorption is weak. The O V line appears in absorption in the observations, and is too strong in the model spectra unless moderately clumped winds ($f \lesssim 0.04$) are assumed. The inclusion of X-rays from shocks in the model strengthens the absorption component of the O VI profile, better matching the observations (see Section 5.2). Our models, with $\log g = 4.8 \pm 0.3$, do a good job at fitting the hydrogen Lyman and helium features in the *FUSE* range (915–960 \AA) as well as the optical absorption lines. Napiwotzki (1999) derived $T_{\text{eff}} = 65 \text{ kK}$, $\log g = 4.8$ based on an optical line analysis for NGC 6058.

4.5 NGC 1535 and 6210

The spectra of both NGC 1535 and 6210 display similar absorption line features from O IV, C IV $\lambda 1169$ and the Fe VI/Fe VII ions, which are well fitted by models with $T_{\text{eff}} \sim 75 \text{ kK}$. The P-Cygni wind lines (S VI, N V, O V, C IV) are adequately fitted by models with $R_t \simeq 2 R_{\odot}$. However, the O VI feature is weak in the models unless X-rays are included in the wind to match the observed strength (Section 5.2). Higher temperature models can fit this feature without the addition of X-rays, however they cannot also fit the C IV feature and He II $\lambda 4686$ simultaneously (with the latter showing unobserved emission when the mass-loss rate is raised to match the former's strength). The mismatch in the continuum between the model and observations of NGC 6210 between $\sim 1100\text{--}1185 \text{ \AA}$ is most likely caused by the worm artefact (Section 2.1). For both stars, using hydrogen Lyman and helium features in the *FUSE* range and the optical absorption lines, we constrain $\log g$ to be 4.8 ± 0.3 (± 0.2 for NGC 6210).

The high-resolution, high S/N UV spectra (*IUE* for NGC 6210, STIS for NGC 1535) allow us to constrain the clumping values from

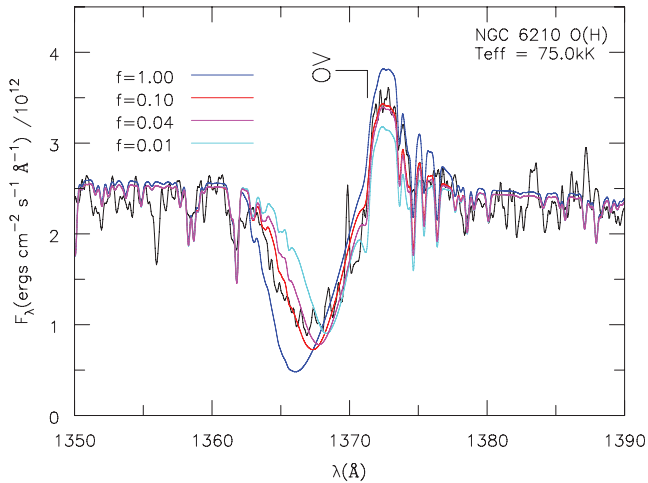


Figure 10. NGC 6210. *IUE* observations of the O v $\lambda 1371.3$ profile (black) along with our models computed with different clumping volume filling factors ($f = 1, 0.1, 0.04$ and 0.01). $f = 1$ corresponds to a smooth wind, while the best-fitting value ($f = 0.1$) corresponds to clump densities 10 times that of the smooth wind.

the O v line. In both cases, clumping values of $f > 0.1$ result in this feature being too strong compared to observations (Fig. 10).

The observed Si iv doublet is stronger than in our model spectra in both cases. For NGC 1535, the high-resolution STIS spectra reveal that both Si iv components display a double-peaked absorption profile, with the stronger component blueshifted by about $\simeq 20 \text{ km s}^{-1}$, as shown in Fig. 8 (the nebula of NGC 1535 has an expansion velocity of 20 km s^{-1} ; Weinberger 1989). Similarly, for NGC 6210, close inspection shows the observed lines blueshifted with respect to the rest wavelength. We believe this indicates these features are mainly due to circumstellar Si iv (also, models with temperatures low enough to fit this feature are totally inconsistent with all other spectral diagnostics). As with LSS 1362, the high-resolution data reveal absorption components associated with the circumstellar material (see Section 5.5).

For NGC 1535, we (Herald & Bianchi 2004b) previously derived $T_{\text{eff}} \simeq 65 \text{ kK}$ and a higher mass-loss rate under the assumption of a smooth wind ($f = 1$) and no shocks. Our parameters derived here provide better fits overall. In Herald & Bianchi (2004b), P-Cygni absorptions were generally too strong, while O vi was too weak.

4.6 NGC 6543: the Cat’s Eye

The spectra of the central star of NGC 6543 (the ‘Cat’s Eye’ nebula) offers a wealth of strong lines spanning multiple ionization stages for many elements. In addition to the N iv, N v, C iii, C iv, O iv, O v, O vi, P v, He ii, Si iv, S vi, Fe v and Fe vi lines, we also were guided by the following diagnostics: N iii $\lambda\lambda 989.8, 991.5$, N iv $\lambda 955.3$, C iv $\lambda\lambda 1198.4, 1198.6$, O iv $\lambda\lambda 923.37, 923.44$, S v 1501.8 . As discussed by Georgiev et al. (2008), many of the strong P-Cygni profiles display significantly different terminal velocities, and the wind of NGC 6543 has been found to be variable (Prinja et al. 2007) (e.g. the blue wing of the C iv doublet fluctuates). It is difficult to achieve a good fit to all these diagnostics simultaneously (note that the far-UV, UV and optical data sets are from different epochs), and so there is a larger uncertainty in the derived parameters for this star with respect to the others. We derive $T_{\text{eff}} = 60_{-5}^{+10} \text{ kK}$, where the uncertainty range is required to eventually achieve good fits to all diagnostics (with the exception of O vi, N v and C iv, discussed

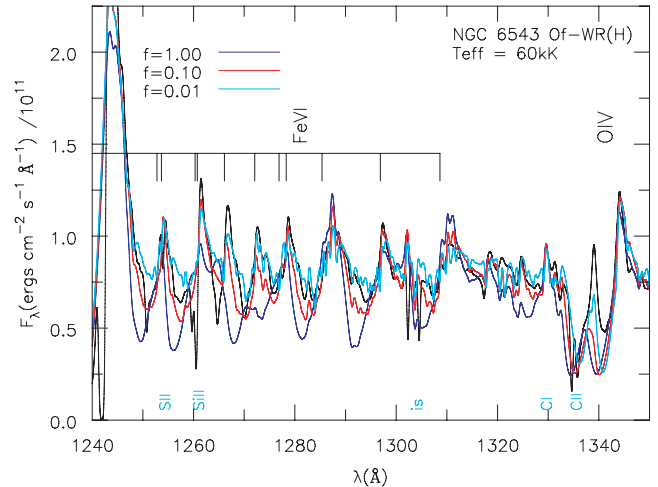


Figure 11. NGC 6543. STIS E140H observations of the Fe vi forest (black) along with our models of different clumping volume filling factors ($f = 1, 0.1$ and 0.01). Using these features, clumping is constrained to be $0.01 \leq f \leq 0.1$. The spectra have been convolved to a resolution of 0.5 \AA for clarity.

below). The cooler model with $T_{\text{eff}} = 55 \text{ kK}$ well fits the C iii $\lambda 977$ line, while the hotter models better fit the Fe vii lines. An upper limit to the mass-loss rate is set by the optical lines, which still leaves the far-UV and UV lines slightly weak. In addition to the P v doublet, the Fe vi spectrum ($\sim 1200\text{--}1350 \text{ \AA}$) is sensitive to the amount of wind clumping, while being fairly insensitive to T_{eff} in this parameter regime. These features constrain the clumping factor to $0.1 < f < 0.01$ (Fig. 11). The models shown in Figs 1–6 and the parameters given in Table 5 are for $f = 0.04$. There are details in the shape of the observed P v profile that our model spectra do not duplicate. Prinja et al. (2007) performed a detailed study of the wind structure of NGC 6543 using time series data, and identified discrete-absorption components which temporarily appear and migrate bluewards across the P-Cygni absorption of the P v line. Such time-dependent structures are not implemented in CMFGEN, but their neglect should not alter the derived parameters. For any parameter combination tested, the He ii $\lambda 1640$ feature was too strong in the models. We have adopted a helium mass fraction of 10 per cent, which better fits the observed helium lines.

We constrained the gravity to be $\log g = 4.7 \pm 0.3$ mainly using the He ii 958.7, 972.1 features. Models without X-rays do not adequately fit the O vi, S vi and N v doublets, which are weaker than observed. We achieved better fits including X-rays in the models, as discussed in detail in Section 5.2.

Georgiev et al. (2008) performed a detailed analysis of NGC 6543 also using CMFGEN. Their derived stellar parameters are in rough agreement with ours, although they relied on a different set of diagnostics.

4.7 The Slow wind of NGC 2392

What distinguishes the spectra of the central star of NGC 2392 (the Eskimo nebula) from those of the rest of our sample are the very narrow absorption components of its P-Cygni features. As can be seen in Fig. 12, the S vi, C iii, C iv, N v and O vi profiles indicate a slow wind, with blue edge of the C iv at $\sim 200 \text{ km s}^{-1}$, as has been noted by Guerrero et al. (2010). Both components of the N v doublet, the blue component of O vi and the red component of S vi display a more gradual absorption extending $\sim 300\text{--}400 \text{ km s}^{-1}$ bluewards (the other components of the latter two are obscured by

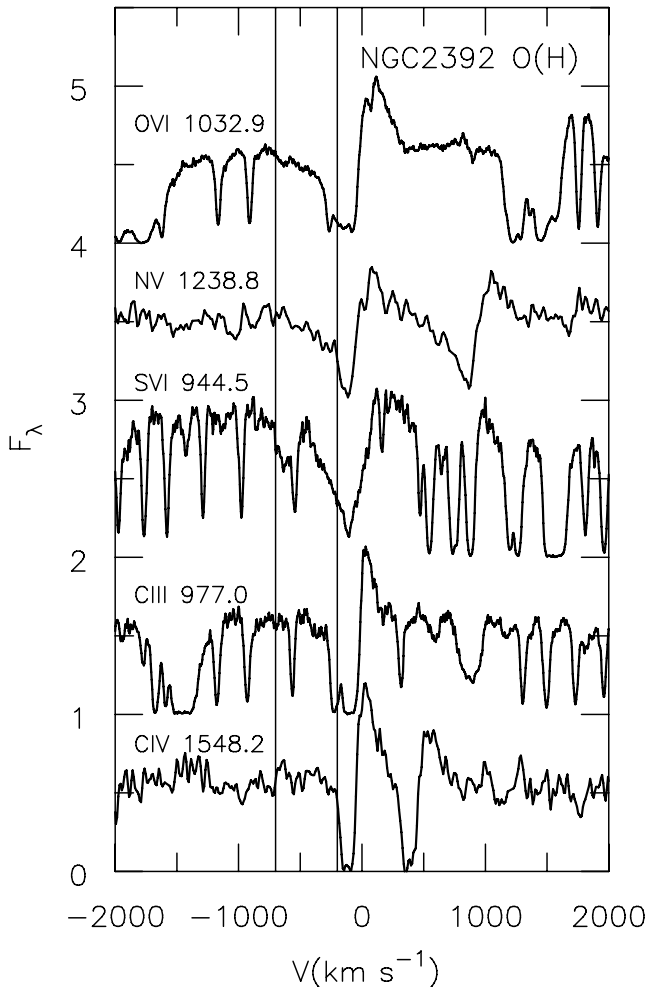


Figure 12. NGC 2392. P-Cygni profiles of O VI, N V and C IV (blue components), S VI (red component) and C III lines in velocity space. The C IV and nitrogen profiles have steep edges at $\approx 200 \text{ km s}^{-1}$, and those of nitrogen, oxygen and sulfur show an additional gradual, more extended absorption component out to $\sim 600\text{--}700 \text{ km s}^{-1}$ (the vertical lines are at 200 and 700 km s^{-1}). The fluxes have been scaled and shifted vertically by arbitrary amounts for illustration.

H₂ absorptions). The gradual absorptions seen in the profiles of the super-ions (Fig. 12) may be the result of shocked material moving at higher velocities than the rest of the wind. Such features are not taken into account in CMFGEN’s treatment at present. We find a value of $v_\infty = 300 \text{ km s}^{-1}$ matches the widths of most emission and absorption components.

Our spectroscopic analysis indicates the metallicity of NGC 2392 is subsolar. The *IUE* spectrum also shows a forest of weak iron features, originating mainly from Fe VI (between 1200 and 1300 Å) and Fe V (between 1300 and 1600 Å). These iron lines, as well as many metal lines of the far-UV and UV spectrum (the Si IV features and S IV $\lambda\lambda 1062.66, 1072.97$), are too strong when solar abundances are assumed. Using these lines, we constrain the metallicity to $z \lesssim 0.25 Z_\odot$ (the models for NGC 1362 shown in this paper have been calculated with this metallicity). Nebular abundances for NGC 2392 were determined by Pottasch, Bernard-Salas & Roellig (2008) from mid-IR spectra. They found O, Ne, S, Ar and Cl abundances depleted by a factor of 2 with respect to solar, consistent with the star’s distance from the Galactic Centre.

Our models with $T_{\text{eff}} \simeq 45 \text{ kK}$ duplicate the fine structure observed in the UV range well, along with the C III 1176 complex. For higher temperatures, the C III feature cannot be reproduced and He II $\lambda 4686$ is too strong for mass-loss rates which match the strength of the other features, while in models cooler than 42.5 kK the carbon features are strong. Models of all of these discussed temperatures, however, are too cool to duplicate the observed O VI and weak S VI profiles at all, and have N V profiles which are weak compared with observations. Inclusion of X-rays in the model winds brings out these features, and we discuss the implications of this more in Section 5.2. The narrowness of the wind features of this star prevents us from firmly constraining the degree of clumping, and so we have assumed $f = 0.1$ in this case. We note that a model with a higher degree of clumping ($f = 0.004$) is required to make the P V strength consistent with observations, but then other features are no longer matched.

The high-resolution *IUE* spectrum presented here was taken in the *IUE* large aperture. Comparison with the two spectra taken through the small aperture indicates that the strong (non-P-Cygni) He II $\lambda 1640$ emission is mainly nebular (we present the large aperture data here because the continuum levels match the *FUSE* data in regions of overlap).

In addition to subsolar metal abundances, we find a peculiar abundance pattern for the CNO elements. A nitrogen abundance of $\sim 3.3 \times 10^{-3}$ (by mass, about three times the solar value) is needed to fit numerous far-UV features, namely N IV absorption features at 955.33, 1133.1, 1135.3 and 1136.3 Å, N III absorptions at 980, 1183, 1184.5 Å, and the N III P-Cygni doublet at 989.80, 991.5 Å. Oxygen must be depleted to $< 1 \times 10^{-4}$ or the following absorption features are stronger than observed: O V $\lambda 1371$, O VI $\lambda\lambda 1338, 1343$, O III at $\lambda\lambda 1150.9$ and 1153.8, and O IV $\lambda 1067.8$. A small reduction in the carbon abundance then fits C III $\lambda 1176$ better, while maintaining a C+N+O mass fraction total consistent with the one-fourth solar metallicity value we have adopted. That the surface of NGC 2392 appears to show a carbon deficiency and nitrogen enhancement has been noted previously by Pauldrach, Hoffmann & Méndez (2004). This abundance pattern may indicate a second dredge-up has occurred, which is expected to result in an increase in N but decreases in C and O (Marigo et al. 2003); however, this is only expected for stars with progenitor masses between 3 and $5 M_\odot$.

Kudritzki et al. (2006) analysed optical spectra of NGC 2392 and obtained $T_{\text{eff}} = 44 \text{ kK}$, $v_\infty = 400 \text{ km s}^{-1}$, $\log g = 3.6$ and $f = 1$, while Pauldrach et al. (2004) derived $T_{\text{eff}} = 40 \text{ kK}$, $v_\infty = 420 \text{ km s}^{-1}$, $\log g = 3.7$ using hydrodynamical models and UV spectra. These are similar to our derived parameters, except we find our lower value of $v_\infty = 300 \text{ km s}^{-1}$ to better match the P-Cygni profiles. In particular, in the model fits presented by Pauldrach et al. (2004), the absorption edge of the red C IV component extends far enough bluewards to totally absorb the blue component, contrary to observations. Our lower v_∞ value allows both components to be duplicated (although the absorption edges extend a bit too far bluewards, even with such a low v_∞ !). We note that NGC 2392 does show photometric variabilities, these are believed to stem from pulsations or wind variability (Miszalski et al. 2009).

Our derived temperatures are lower than those derived from nebular diagnostics (70–80 kK; Tinkler & Lamers 2002; Pottasch et al. 2008). It has been suggested that the high ionization of the nebula is caused by a companion object (Heap 1977), although as of yet no firm detection has occurred, and there is no obvious indication of a hotter companion in the *FUSE* spectrum.

4.8 IC 4593

$S\text{ VI}$, $C\text{ III}$, $O\text{ VI}$, $P\text{ V}$, $N\text{ V}$, Si IV and $C\text{ IV}$ as well as $C\text{ III } \lambda 1175$ all present P-Cygni wind profiles in the spectra of IC 4593. The rich spectrum of absorption features seen in the high-resolution *IUE* spectrum between 1200 and 1700 Å arises from Fe V , and the $O\text{ IV}$ feature appears in absorption. Our models with $T_{\text{eff}} \sim 41\text{ kK}$ fit this region well, despite its complexity, while also adequately fitting the far-UV $C\text{ III}$ and $S\text{ VI}$ wind features. For models hotter than $T_{\text{eff}} > 42.5\text{ kK}$, the far-UV $C\text{ III}$ features are too weak, and the optical $\text{He II } 4684$ line too strong, while for models cooler than $T_{\text{eff}} < 40\text{ kK}$, the $C\text{ III}$ and Si IV features are too strong. We determine $\log g = 3.7 \pm 0.2$, mainly from the optical spectrum.

The P-Cygni absorption edges of the strong wind lines span a large range of terminal velocities. For example, the $O\text{ VI}$ feature indicates $v_{\infty} \simeq 1000\text{ km s}^{-1}$ while $C\text{ III } \lambda 1176$ indicates $v_{\infty} \simeq 700\text{ km s}^{-1}$. We have computed two final models for this star, with $v_{\infty} = 750$ and 1000 km s^{-1} . R_1 is preserved in both models, so they have slightly different mass-loss rates. Both fit the strengths and profile shapes equally well, aside from the variance in the absorption edges of the P-Cygni lines. We will refer to these models later (Section 5.1) for purposes of illustration. In Figs 1–6 we present the $v_{\infty} = 750\text{ km s}^{-1}$ model.

Using the $P\text{ V}$ feature, clumping is constrained to be $0.01 \leq f \leq 0.1$ (see Fig. 13). Not well fitted by our adopted non-X-ray model are the $O\text{ VI}$ P-Cygni profile (not present at all in the model spectrum) and the $N\text{ V}$ doublet (too weak in the model). To attempt to fit these lines, we calculated exploratory models with varying amounts of X-rays in the wind, which we discuss in Section 5.2. In all our models, the $C\text{ IV}$ line is too weak, however increasing the carbon abundance does not substantially improve the fit (as it is saturated) while rendering the $C\text{ III } 1175$ line strong. One possibility for the discrepancy is that IC 4593 shows photometric variability (Miszalski et al. 2009), believed to stem from pulsations or wind variability, rather than from a close companion.

Kudritzki et al. (2006) analysed optical spectra of IC 4593 to obtain $T_{\text{eff}} = 40\text{ kK}$, $v_{\infty} = 900\text{ km s}^{-1}$, $\log g = 3.6$ and $f = 0.25$, while Pauldrach et al. (2004) derived $T_{\text{eff}} = 40\text{ kK}$, $v_{\infty} =$

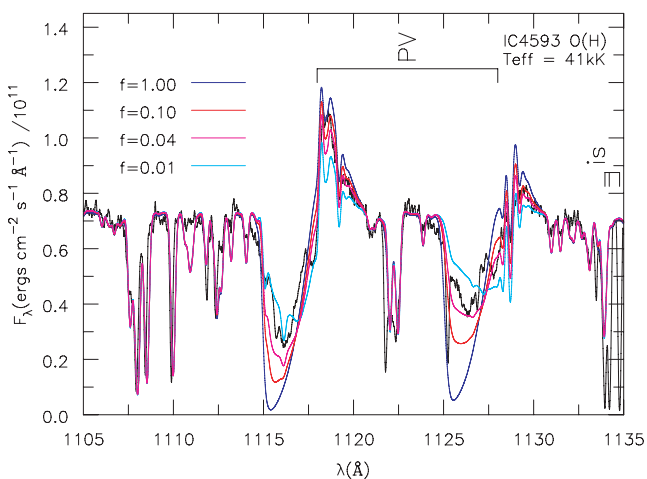


Figure 13. NGC 4593. *FUSE* observations of the $P\text{ V } \lambda\lambda 1118, 1128$ profile (black), along with our $v_{\infty} = 750\text{ km s}^{-1}$ models (see text) of different clumping volume filling factors ($f = 1, 0.1, 0.04$ and 0.01). Using this feature, clumping is constrained to be $0.01 \leq f \leq 0.1$. $f = 1$ corresponds to a smooth wind, while the best-fitting value ($f = 0.04$) corresponds to clump densities 25 times that of the smooth wind.

850 km s^{-1} , $\log g = 3.8$ using hydrodynamical models to analyse UV spectra.

5 OTHER RESULTS

Here we discuss results which apply more generally to H-rich CSPN and their winds. Namely, clumping, X-rays, the circumstellar environment and the importance of many trace elements in the model atmospheres.

5.1 Wind clumping

In this section, we discuss our findings concerning clumping in the winds of these H-rich CSPN. As explained in Section 3.1.1, we initially adopted a clumping factor of $f = 0.1$ for our models (i.e. assumed a wind consisting of clumps with a density 10 times that of the smooth-wind density). Some of our sample stars display spectral features known to be sensitive to clumping in the winds of massive stars (Bianchi et al. 2009). For these stars, we computed models with different clumping factors, and found that some of our sample stars required a higher degree of clumping to fit certain spectral features, as we now discuss.

For NGC 6210 and 1535, the $O\text{ V } \lambda 1371$ line, particularly the absorption component, was too strong when clumping $f > 0.1$ was adopted. We computed models (preserving R_1) with $f = 1, 0.1, 0.04$ and 0.01 , as illustrated in Fig. 10. We found $f = 0.1$ to produce the best fits (other wind features were only affected in minor ways). Although the $O\text{ V}$ feature is present in the spectra of IC 2448, it is weaker in this star, and the S/N of the spectra are too low to place constraints on the clumping. For NGC 6058, the $O\text{ V}$ feature appears in absorption, which could only be duplicated using $f \leq 0.04$.

In the case of NGC 6543, the forest of unsaturated Fe VI UV lines also reacts to the wind clumpiness. We derived $0.1 < f < 0.01$, with $f \simeq 0.04$ producing better fits overall (Fig. 11). Prinja et al. (2007) derived $f = 0.08$, also using *CMFGEN* and the $P\text{ V}$ profiles.

The $P\text{ V}$ lines of IC 4593 were too strong in models with $f = 0.1$ where the strengths of the other spectral features were matched adequately. Again, testing a range of values constrained clumping to $0.04 > f > 0.01$ (Fig. 13), with 0.04 appearing to produce the best fit.

For our other sample stars without useful clumping spectral diagnostics (NGC 7662, LSS 1362, NGC 1360 and IC 2448), we were able to achieve good quality fits assuming $f = 0.1$; however, the few wind lines these stars present are not particularly sensitive to the clumping parameter.

We also found that initiating clumping at relatively low velocities ($10\text{--}50\text{ km s}^{-1}$ rather than hundreds of km s^{-1}) provided the most consistent model profiles compared to observations. This parameter affects line profiles as clumping enhances emission at high velocities relative to that at lower velocities. An example is shown in Fig. 14, for which $v_{\text{clump}} < 50\text{ km s}^{-1}$ were required to match the $C\text{ III}$ features at 1176 Å . We adopted $v_{\text{clump}} = 10\text{ km s}^{-1}$ for this star as well as NGC 2392 ($v_{\infty} \simeq 300\text{ km s}^{-1}$). For the stars of our sample with faster winds (i.e. $> 1000\text{ km s}^{-1}$), we found that $v_{\text{clump}} = 50\text{ km s}^{-1}$ better matched details of the line profile shapes (with smaller values $50 > v_{\text{clump}} \geq 10\text{ km s}^{-1}$ not offering significant improvements). The low values for v_{clump} we derive for these CSPN are similar to the results of Hillier et al. (2003), who found that for O supergiants, $v_{\text{clump}} = 30\text{ km s}^{-1}$ based on the profile of the $H\alpha$ line.

To summarize, the high-resolution far-UV and UV spectra utilized in our analysis allowed us to well constrain clumping in the

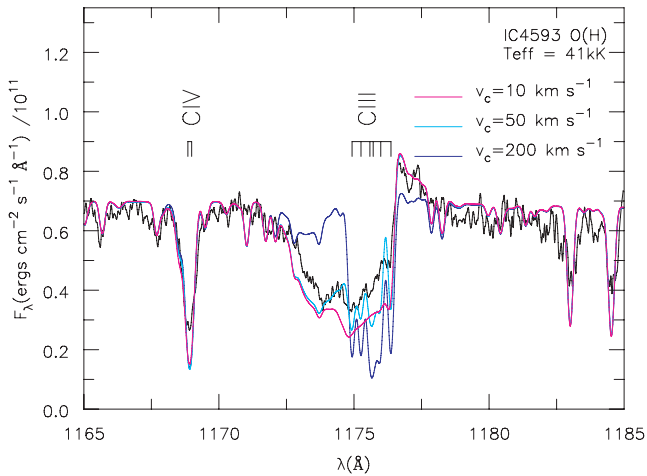


Figure 14. NGC 4593. *FUSE* observations of the C III $\lambda 1176$ multiplet profile (black), along with our $f = 0.04$, $v_\infty = 750 \text{ km s}^{-1}$ model (see text) computed with clumping starting at wind velocities of $v_{\text{clump}} = 10, 50$ and 200 km s^{-1} (pink, aqua and blue). These velocities correspond to $\sim 1.1, 1.2$ and $1.5 R_*$. Unless clumping is initiated at low velocities, the photospheric component is too strong and the wind absorption does not extend blueward enough compared with observations.

winds of H-rich CSPN using the P v and (for the first time) O v and iron features. For these stars, (spanning $\sim 40\text{--}80 \text{ kK}$) clumping was found to be $0.1 \lesssim f \lesssim 0.04$. We were also able to achieve acceptable fits for the other stars of our sample assuming $f = 0.1$. These results seem to indicate the winds of H-rich CSPN are highly clumped, characterized by clump densities 10–25 times that of the smooth-wind value. This effectively reduces derived mass-loss rates for these objects by one-third to one-fifth their smooth-wind values, of consequence to nebular dynamics and interstellar enrichment studies.

We note that these revised mass-loss rates are contingent on the assumption of optically thin clumps to be correct. Alternative models of clumping structure, with the assumption of optically thick clumps (Oskinova, Hamann & Feldmeier 2007) have been used to successfully match the wind diagnostics of ζ -Puppis, without requiring a reduction in mass-loss rate compared to the smooth-wind models. However, X-ray results which probe the winds of ζ -Puppis indicate a clumping structure more in accordance to the optically thin model (Cohen et al. 2010). Which model is more appropriate for the various classes of stars with winds (WR, O, CSPN) remains an open question.

5.2 X-Ray flux in the wind

Despite the wide temperature range covered by the 10 CSPN analysed here (40–120 kK, see Table 5), all objects show the high-ionization O v i doublet as a P-Cygni profile (although that of NGC 1360 is weak). For the two coolest stars (NGC 2392 and IC 4593), the appearance of this feature (and also the strength of the N v doublet) is totally inconsistent with the other spectral features, which indicate stellar temperatures of $T_{\text{eff}} \leq 45 \text{ kK}$. We were able to match the strength of the observed O v i feature by adding an additional source of X-rays, as shown in Fig. 15. For the intermediate-temperature stars ($55 \gtrsim T_{\text{eff}} \gtrsim 90 \text{ kK}$), the model O v i doublets were weak without an assumed X-ray source, the addition of which improved the fit without altering the other spectral features (again,

see Fig. 15). Only for the hottest stars ($T_{\text{eff}} \gtrsim 90 \text{ kK}$) were X-rays unnecessary to fit all the high-ionization features displayed in their spectra.

We often found it difficult to simultaneously fit the N v and O v i lines. Since a detailed analysis of the shocked wind structure is beyond the scope of this paper, our strategy was to adjust the X-ray filling factors to fit only the O v i line. We initiated X-rays at the same velocities as we initiated clumping (Section 5.1), i.e. $v_x = 10 \text{ km s}^{-1}$ for stars with $v_\infty < 1000 \text{ km s}^{-1}$ and $v_x = 50 \text{ km s}^{-1}$ for the rest.

Fig. 16 shows the effect of including X-rays in the model atmosphere calculation on the wind ionization structure of oxygen for NGC 6543. The addition of X-rays increases the ionization fraction of O v i in the outer parts of the wind, without significantly changing the ionization structure of the lower ionization species. This allows the observed strength and of the O v i $\lambda\lambda 1032, 38$ line to be matched without affecting the strength of the lower ionization features.

Table 5 lists the predicted observed X-ray luminosities ($>0.1 \text{ keV}$) for our best-fitting models for each star, as well as for the equivalent non-winds-X-ray model (for which the X-ray emissions would be purely photospheric). One can see the X-ray luminosities jump by several magnitudes between 55 and 75 kK, and again between 80 and 95 kK for the non-winds-X-ray models. When X-rays were included to reproduce the O v i feature in stars of $T_{\text{eff}} < 80 \text{ kK}$, X-ray fluxes above 0.1 keV of $L_x/L_* = \text{a few} \times 10^{-5}$ were typically required. We found that X-ray fluxes three times weaker were inadequate to match O v i, while fluxes three times larger would dramatically change the ionization structure of the wind causing nearly all model spectral features to fail to match the observed strengths. Lines used in this work to constrain X-rays are insensitive to clumping and vice versa, to avoid degeneracies in the derived parameters.

The required X-ray luminosities we derive for our sample CSPN are higher than the $\log L_x/L_* \simeq -7.0$ typically observed for O stars (Chlebowski & Garmany 1991). The development of a more sophisticated treatment of X-rays by CMFGEN is ongoing, as discussed by Zsargó et al. (2008). Using an enhanced version of CMFGEN, they found, for the wind of the supergiant ζ -Puppis (O5Iaf), that accounting for the contribution from the tenuous interclump medium as well as from the denser clumped regions was necessary to reproduce the observed O v i profile of this star. They also found that the interclump region played a varying role in the formation of other lines for that star: the main contribution of C iv is from the densest regions of the wind, while for O v i it is from the interclump region, while N v is an intermediate case. Although such work has yet to be extended to the winds of CSPN, it is likely, given the commonalities that have been found between the winds of massive stars and of CSPN, that such effects play a similar role for CSPN. Thus, the neglect of the interclump medium when fitting the O v i profile most likely overestimates the required X-ray luminosity. Given the current poor state of knowledge about X-ray and clump formation in CSPN winds, our main goal was to show that X-rays from shocks could indeed be a plausible explanation for the strength of high-ionization features in cooler stars, leaving a more sophisticated treatment for the future.

Only ~ 25 PN systems have been observed with modern X-ray observatories such as *Chandra* and *XMM-Newton*. Of these, nine have been detected as diffuse X-ray sources while even fewer have been detected as point sources (see Kastner 2007, for a review, and references therein). Even then, there are other possible sources of X-ray emission than shocks in the stellar wind, such as from

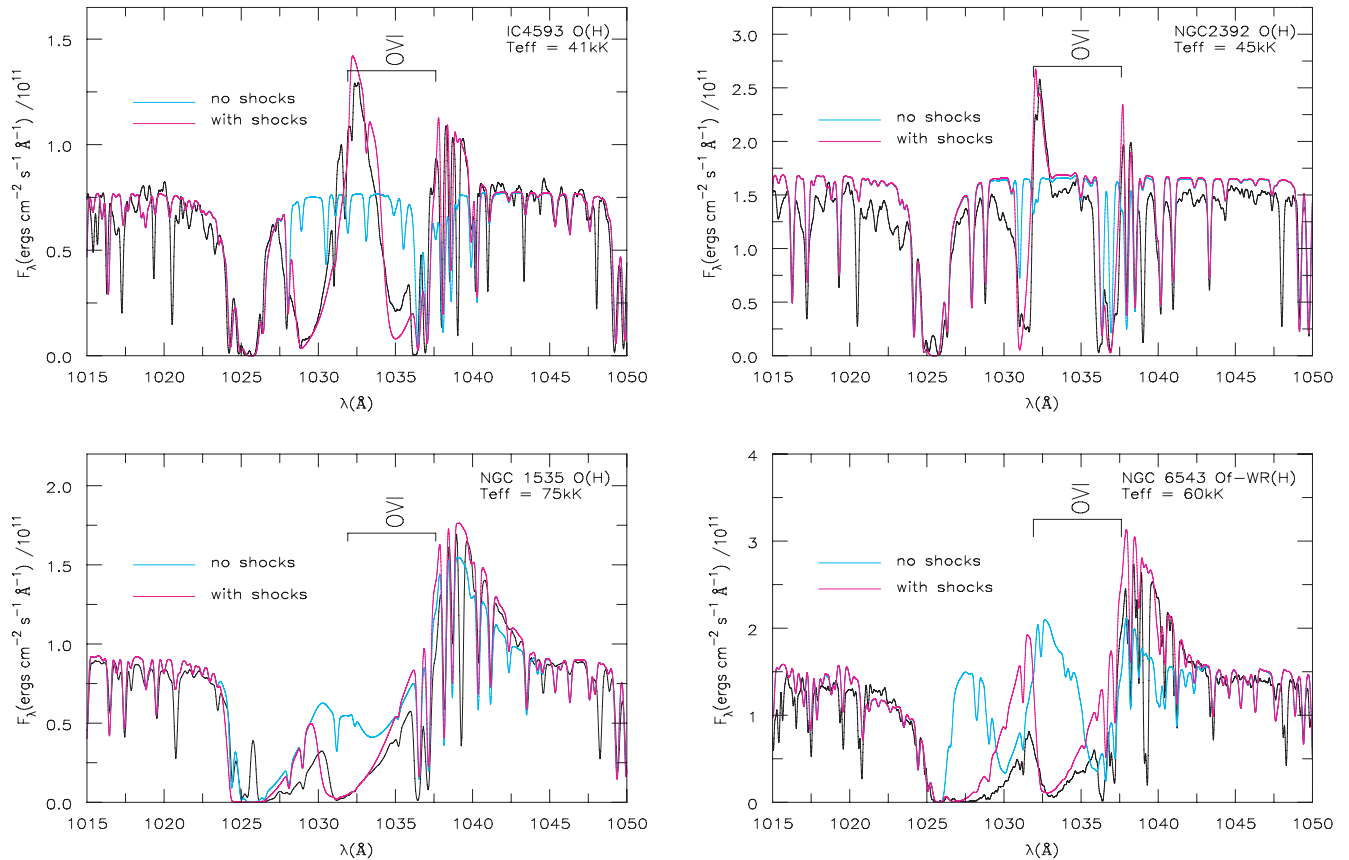


Figure 15. O VI *FUSE* observations of the O VI $\lambda\lambda$ 1032, 1038 profile (black) for IC 4593, NGC 2392, 1535 and 6543, along with our best-fitting models for those stars calculated with/without (pink/aqua) X-rays from shocks. The profiles of IC 4593 and NGC 2392 are not reproducible at all without including an X-ray component, while those of NGC 1535 and 6210 are better matched when one is assumed, for stellar parameters consistent with the other line diagnostics.

shocks of the fast stellar wind interacting with the slower moving nebular material close to the central star. Of our sample stars, NGC 6543 and 2392 have been detected as X-ray source. For both, the origin of the X-ray emission is unclear. NGC 6543 has been detected both as diffuse and point X-ray source. Guerrero et al. (2001) measured an X-ray flux (0.3–2.0 keV) of 10^{30} erg s $^{-1}$ ($2.6 \times 10^{-4} L_{\odot}$), which they believed to be likely coming from a point source associated with the central star. They suggested this X-ray emission to originate either from shocks in the stellar wind or perhaps from coronal activity of a masked binary companion (which has been invoked to explain the observed precessing collimated outflows; Miranda & Solf 1992; Harrington & Borkowski 1994). Chu, Gruendl & Guerrero (2004) suggested that the O VI ions are created in thermal collisions at the interface between the hot interior gas and the cool nebular shell. Fig. 2 shows a model which matches the observed strength of the O VI profile (although the shape is not perfect) without unduly altering the fits of the other features. Assuming, as did Guerrero et al. (2001), that the distance to NGC 6543 is 1 kpc (Table 1), our derived luminosity is $L_{*} = 1.55 \times 10^{-3} L_{\odot}$, while the predicted X-ray luminosity (i.e. flux not absorbed by the wind) is $L_x \simeq 5 \times 10^{-3} L_{\odot}$, about 20 times higher than measured by Guerrero et al. (2001) (but, as discussed above, the current implementation of X-rays most likely overestimates the required X-ray flux).

Guerrero et al. (2005) studied the X-ray emission from the Eskimo nebula with the *XMM-Newton* instrument, and found it to be extended but confined to the inner shell, with some harder X-ray emission (0.6–2.0 keV) where the fast bipolar outflow is interacting

with the nebular material. They concluded the high thermal pressure from the hot gas was responsible for the observed high expansion velocity of its innermost shell. However, they were unable to firmly identify the origin of the hot gas, suggesting it may consist of several components: the shocked fast stellar wind, shocks associated with the fast bipolar flow, or possible emission from its central star or binary companion. We downloaded an archive *Chandra* observation of NGC 2392 which appears to show the CS being a point source of both hard and soft X-ray emission. Our X-ray models demonstrate stellar wind shocks are a plausible explanation consistent with the observed spectra.

To summarize, although there are other explanations for the origins of the intra-wind X-ray fluxes (wind interactions with an undetected companion), a more natural explanation is that clumped winds and intra-wind shocks may be a characteristic of CSPN winds. In cooler objects, these shocks are responsible of the observed high-ionization features. In hotter stars, X-rays from shocks may be present, but photospheric X-ray emission dominates and is primarily responsible of O VI and N V. In the winds of stars of intermediate temperatures (~ 50 – 90 kK), both X-ray sources may play significant roles in the creation of such lines.

We conclude this section by noting our fits to shock-influenced lines such as O VI do not allow rigorous determinations of X-ray parameters (such as X-ray luminosity), as our assumptions regarding the temperature and structure of the shocks in the wind are somewhat ad hoc. However, our results do illustrate the necessity of invoking X-rays from shocks to fit of some features (O VI, S VI, N V) consistently with other spectral diagnostics, resolving otherwise

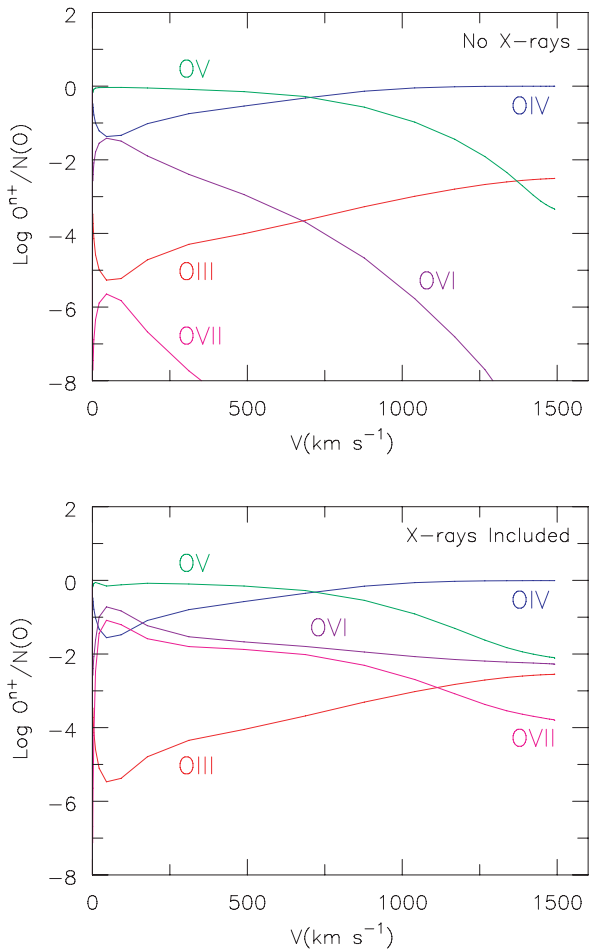


Figure 16. Ionization structure of oxygen of model atmosphere for NGC 6543, both with (bottom) and without (top) X-rays included in the calculations (these correspond to the model shown for NGC 6543 in Fig. 15). The ionization fractions as a function of wind velocity are shown for O III–O VII (red, blue, green, purple and pink, respectively). The addition of X-rays boosts the ionization fraction of O VI in the outer parts of the wind, necessary to match the O VI $\lambda\lambda 1032, 38$ profile, without significantly changing the ionization structure of the lower ionization species.

irreconcilable inconsistencies in the spectral diagnostics. Finally, the inclusion of X-rays in our models of the hotter stars of our sample shows that their neglect would not alter parameter determinations above certain temperatures, as the photospheric radiation field dominates in setting the populations of the high-ionization features.

5.3 Trace elements in the model atmospheres

The high-resolution *FUSE* spectrograph coupled with atomic data for high-ionization species has led to the identification of many new diagnostic absorption lines in hot CSPN. Examples include Ne VII $\lambda 973.3$, Ne VIII $\lambda 1165$, Ar VII $\lambda 1063.5$, F VI $\lambda 1139.5$, Ca X $\lambda\lambda 1137, 1159$ (Werner et al. 2004; Werner, Rauch & Kruk 2005, 2007a,b, 2008). Some of these have been observed as P-Cygni wind lines in H-deficient CSPN (Ne VII $\lambda 973.3$ – Herald et al. 2005, Ar VII $\lambda 1063.5$ – Herald & Bianchi 2009). Surface abundances of these elements in CSPN may reflect the final intershell composition of the AGB phase, thus offering clues into the evolution of this class of stars (see Werner & Herwig 2006, for a review). Motivated by these considerations,

we investigated the effects of including many elements in our stellar atmosphere models that have been neglected in prior CSPN studies. A secondary motivation is to test the assumption that such elements have a relatively minor influence in the stellar atmosphere, and so can be safely neglected when determining parameters other than their abundances.

As mentioned in Section 3.1.3, it is currently not feasible to calculate stellar atmosphere models which include all available atomic data due to limitations in computer speed and memory. Therefore, we determined stellar parameters (e.g. T_{eff} , M) using models which included the more important elements: H, He, C, N, O, Ne, Si, P, S and Fe. We then calculated models with additional elements on an individual basis. These elements include Na, Mg, Al, Cl, Ar, K, Ca, Cr, Mn, Co and Ni. Many of these (Na, Al, Cl, K, Cr, Mn, Co) had no significant impact on the model spectra, neither the continuum level nor on the spectral features of the other elements. The inclusion of Mg, Ca, and Ni, however, did change the continuum levels by at most 2 per cent (which would translate into slightly different derived radius, luminosity, etc). This change is caused by the numerous blanketing transitions these elements have shortward of 900 \AA . Although some of the tested elements showed spectral features between 900 and 3300 \AA , at solar abundance they were typically too weak to make a firm correlation with observed features (the majority occurring in the *IUE* long-wavelength range, where spectral S/N is poor).

One exception is argon, which presents a moderately strong spectral feature in many of our model spectra. This line, Ar VII $\lambda 1063.55$, was identified in absorption by Werner et al. (2007a) in several hot ($T_{\text{eff}} = 95\text{--}110 \text{ kK}$) CSPN and used to constrain their argon abundance. The argon abundance in the intershell region of AGB stars is expected to be unchanged, based on nucleosynthesis calculations. For NGC 1360 (the common object in both samples), they found a marginal Ar overabundance within the error limit to the solar value. We also find a solar argon abundance is adequate for NGC 1360. However, we find this feature appears at moderate strength in the model spectra of most of our other stars, but it is too blended with H_2 absorptions in most cases to make an abundance determination (LSS 1362, NGC 7662, 6210 and 6058). In the spectrum of NGC 1535, it is the stronger component of the blend, and the solar abundance value appears consistent with the observations. For IC 2448, although the model Ar VII feature appears weak in Fig. 1, the observed absorption feature is actually a blend of the $\lambda 1063.55 \text{ \AA}$ argon line, and a stronger unidentified feature at 1063.3 \AA when seen at full resolution. We also find this Ar VII line appearing as a P-Cygni profile in the spectrum of NGC 6543 (Fig. 17). Thus, the Ar VII feature may be present in stars with $T_{\text{eff}} \gtrsim 55 \text{ kK}$. The models shown in Figs 1–6 were computed with argon included in the model atmospheres.

Another element which has a noticeable influence on the synthetic spectra (mainly of the cooler stars) was nickel, which tended to improve the fits between $\sim 1250\text{--}1500 \text{ \AA}$, where numerous transitions from Ni IV–Ni VI appear.

5.4 Evolution

According to traditional models of post-AGB evolution (e.g. Schoenberner 1983), H-rich CSPN are thought to be burning hydrogen under ‘quiet’ conditions, i.e. they start their evolution in thermal equilibrium and the CSPN phase takes place between two successive thermal instabilities or pulses (in contrast to H-deficient CSPN, for which the evolution is more complicated). These models predict that most Galactic (H-rich) CSPN evolve across the HR

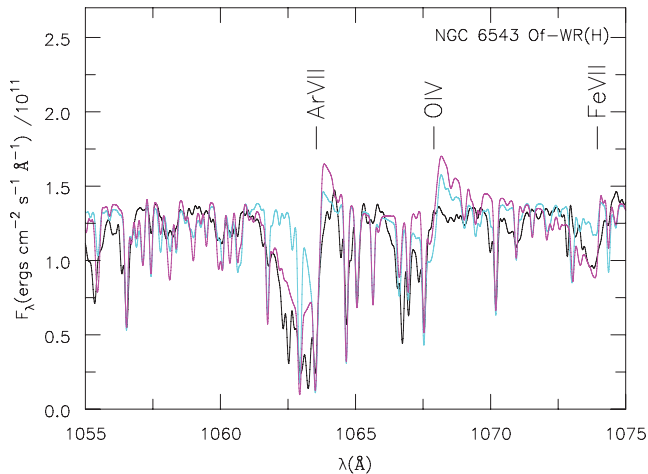


Figure 17. NGC 6543. *FUSE* observations of the Ar VII $\lambda 1063.55$ profile (black) along with models of different temperatures: $T_{\text{eff}} = 55$ kK (aqua) and $T_{\text{eff}} = 65$ kK (pink) (other parameters are the same as our final model, but with $f = 0.1$ and R_1 preserved). The figure illustrates the potential utility of the Ar VII profile as a wind diagnostic.

diagram with $L \simeq 5000 L_{\odot}$, eventually becoming white dwarfs of mass $M \simeq 0.6 M_{\odot}$ (with a lower limit of $L \simeq 2500 L_{\odot}$ for a corresponding final mass of $0.55 M_{\odot}$).

However, agreement between stellar parameters predicted by evolutionary models with those attained by modelling observed spectra with stellar atmosphere codes has proved elusive. A severe hindrance in the analysis of Galactic CSPN is the lack of solid distance determinations for the majority of cases, which means distance-dependent parameters such as R_{eff} and L_* cannot be determined absolutely. That CSPN are shrouded in winds only further complicate the issue. Two studies illustrate the problem. Kudritzki et al. (2006) studied nine H-rich CSPN, determining $\log g$ from optical spectra and using the mass–luminosity relation for post-AGB stars from evolutionary tracks to determine the distance spectroscopically. Pauldrach et al. (2004) analysed the same sample of stars using hydrodynamical codes to model their UV spectra. As summarized by Hamann (2010), both methods resulted in luminosities larger than $10^4 L_{\odot}$, larger than predictions by evolutionary models.

We compared the parameters we have derived with evolutionary models. Distances to almost all of our sample objects are poorly constrained when known at all. There are no distance measurements (other than statistical, which we do not make use of here) for IC 4593, LSS 1362, NGC 6058. The *Hipparcos* parallax measurement for NGC 1360 implies a (highly uncertain) distance of $D = 0.35^{+1.00}_{-0.18}$ kpc, and Ciardullo & Jacoby (1999) determined $D = 2.31$ kpc for NGC 1535 based on its probable association with a main-sequence G-type star. One method for determining distance to a CSPN is based on the expansion parallax of its PN. Such expansion parallaxes have been measured for half of our sample: NGC 7662, IC 2448, NGC 6210, 6543 and 2392 (values and references are listed in Table 1). We note these can be rather imprecise, e.g. Hajian & Terzian (1996) determined $d = 0.79 \pm 0.75$ kpc for NGC 7662.

Our derived model parameters adopting these distances are given in Table 5. Half of the sample lie well below the luminosities predicted by the evolutionary tracks for the CSPN phase, the cut-off of which is $\log L_* \gtrsim 3.5 L_{\odot}$. The masses for all but one case are unrealistically small. Three stars with discrepant parameters have distances derived from expansion parallax velocities. There is reason

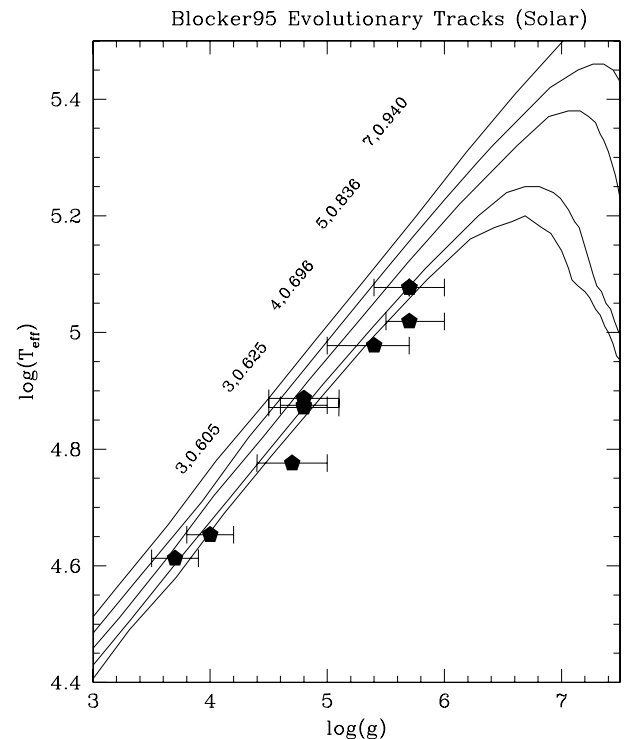


Figure 18. H-burning (solid) tracks of Blöcker (1995) and our model results. Track labels correspond to initial–final masses.

to believe that this method may underestimate distance measurements (by up to a factor of 2; see Steffen et al. 1997; Schönberner & Steffen 2003; Pauldrach et al. 2004, for a discussion). The disagreement with our model parameters and the evolutionary predictions are most probably indicative that the distance determinations need to be refined, rather than of an actual disparity with the evolutionary models.

In Fig. 18, we show our derived temperatures as a function of gravity along with the hydrogen-burning, solar metallicity evolutionary track predictions from Blöcker (1995). The derived parameters lie on the tracks given the uncertainties in the gravity, and indicate low masses for the sample, consistent with the adopted $M \simeq 0.6 M_{\odot}$ in Table 5. Unfortunately the situation prevents us from making any firm conclusions regarding the agreement between our derived parameters and those of the evolutionary models. Assuming $M = 0.6 M_{\odot}$, we derive distances consistently larger than literature values, for all the sample, by factors between 1.5 and 2.5.

5.5 The circumstellar environment

In the high-resolution UV spectra of three stars from our sample (NGC 1360, LSS 1362 and NGC 1535), we identified absorption lines from high-ionization species, blueshifted with respect to the rest wavelength of the CSPN (again, see Fig. 8). Holberg, Barstow & Sion (1998) identified similar high-ionization spectral absorption features at non-photospheric velocities in the spectra of hot ($T_{\text{eff}} \geq 70$ kK) DO white dwarfs. Holberg, Barstow & Sion (1999) argued an interstellar origin for these features can be excluded because they are uncharacteristic of the local interstellar medium, and such features are not observed along adjacent sightlines to stars at greater distances. Bannister et al. (2003) detected such features in the spectra of several DA-type white dwarfs, some of which exhibited multiple-component absorption profiles. They found the

velocities of the shifted components to be consistent with typical expansion velocities of old PNe. Thus, the likely explanation for these absorption features is the stars are ionizing the material of their evolved nebula, which is itself too tenuous and dim to be identified as PNe. Bianchi & Grewing (1987) postulated that the absorption lines velocity-shifted with respect to the central star NGC 40 could be associated with material from its PN. McCandliss & Kruk (2007) used similar profiles to map the velocity structure of the nebular material for the Dumbbell system (NGC 6853), definitively demonstrating their nebular origin. That many of the high-resolution spectra of CSPN seem to have such features suggests these profiles may actually be waiting to be revealed for most CSPN by high-resolution spectrographs [such as from *HST*'s Cosmic Origins Spectrograph (COS)], and offer great potential to disentangle and understand the many elements of these complex systems. It should also be noted, if such nebular absorption lines are present, that analysis of low-resolution spectra would overestimate the photospheric line strengths if they are assumed to be entirely stellar in origin.

6 CONCLUSIONS

We have modelled the spectra of a sample of 10 hydrogen-rich CSPN using *CMFGEN*, a state-of-the-art stellar atmosphere code. The stars are found to span a wide temperature range of 40–120 kK, while the terminal velocities of their winds range from 300 to 2400 km s⁻¹. Comparison of our derived parameters with predictions from evolutionary theory is hindered by poor knowledge of the distances to our sample stars. In particular, using distances derived from nebular expansion parallaxes results in great disagreement with theory in most cases, and most likely indicates (as others have noted) that the expansion parallax method underestimates distances and needs to be refined. When our parameters are scaled assuming a canonical CSPN mass of 0.6 M_⊙, clumped mass-loss rates range from $\sim 3 \times 10^{-8}$ to 1×10^{-9} M_⊙ yr⁻¹ (excluding NGC 1360). For the first time in CSPN analyses, we constrain the clumping parameter, f , using the O v $\lambda 1371$ line. For the cooler stars of our sample, we also use the P v $\lambda \lambda 1118, 28$ and iron lines. Based on these, the winds of H-rich CSPN appears to be characterized by a moderate to high degree of clumping, $0.04 \geq f \geq 0.1$. This indicates that mass-loss rates for this class of objects probably need to be revised to one-third to one-fifth the smooth-wind values, a finding of significant consequence to nebular dynamics, stellar and galactic evolution. We also find that clumping appears to begin at low wind velocities, at radii of $\leq 1.2 R_*$. These results are similar to what has been found for massive O stars.

Additionally, we find it necessary to include X-rays, presumably from shocks, in the model atmospheres to reproduce the features from high-ionization super-ions (O v_i, N v_i and S v_i) present in the spectra of the cooler stars of our sample ($T_{\text{eff}} < 50$ kK). For stars of $50 \leq T_{\text{eff}} \leq 90$, the models underpredict these features unless X-rays are included. Considered with the clumping results above, these results suggest that clumping and X-rays originating from a shocked wind may be a common characteristic of H-rich CSPN winds.

We also tested the effects of including numerous trace elements up to high-ionization stages, hitherto neglected in CSPN analyses. We find new wind diagnostics for H-rich CSPN: Ne v_{ii} $\lambda 973$ and Ar v_{ii} $\lambda 1064$, which may be useful in constraining temperature and mass-loss rates and abundances. Most other elements tested had at most minor effects on commonly utilized diagnostic lines of the model spectra, and therefore may be safely neglected when constraining most parameters. However, line-blanketing elements

such as Mg, Ca and Ni did result in difference of up to 2 per cent in continuum levels.

We are able to produce acceptable fits to most of the major spectral features of our sample assuming solar abundances. One exception is NGC 2392, for which we find a subsolar metallicity ($z \sim 0.25 Z_{\odot}$), as well as a nitrogen overabundance and carbon and oxygen deficiencies. This abundance pattern may partially explain why NGC 2392 has one of the lowest terminal wind velocity (~ 300 km s⁻¹) of any known CSPN to date, as the efficiency of radiative-to-wind momentum transfer is believed to be strongly dependent on the star's metallicity.

Our detailed analysis of the high-resolution spectra also allowed a (previously undetected) weak stellar wind of NGC 1360 to be discerned from its O v_i profile. We constrain its mass-loss rate to be $\lesssim 1 \times 10^{-10}/3 \times 10^{-10}$ M_⊙ yr⁻¹ (clumped/unclumped), the lowest known for a CSPN. This star is thus an important example of a star just leaving the CSPN stage as it turns on to the white dwarf cooling sequence.

We have also identified, from the high-resolution UV data of some stars (NGC 1350, LSS 1362 and NGC 1535), the signature of nebular absorption lines. Such data sets may potentially be used to map the velocity structure of the nebular material and provide an important test the standard interacting wind model of PN evolution (McCandliss et al. 2007; McCandliss & Kruk 2007).

There is room for improvement. In a few cases, the terminal velocities of many strong wind features of a given CSPN varied significantly, and we were unable to fit these simultaneously with a single model. These differences are most likely linked to the details of the clumping and shocked structure of the wind, areas which we are only just beginning to gain insights into for CSPN.

ACKNOWLEDGMENTS

We thank John Hillier for his help with his *CMFGEN* code, and Thierry Lanz and Ivan Hubeny for their help with their *TLUSTY* code. We also thank Stan Owocki for discussing wind structure issues with us, as well as Stephan McCandliss for making his H₂ molecular data available. We also thank the anonymous referee, who provided many useful comments that we feel have strengthened this paper. We greatly appreciate the optical spectra provided to us from Orsola DeMarco, Howard Bond and Melike Afsar. We acknowledge that without the efforts to calculate atomic data of the *OPACITY* project, this work would not have been possible. The *SIMBAD* data base was used for literature searches. This work has been funded by NASA grants NNX07AH39G (06-ADP06-40) and (HST-AR-11256.01A). The *FUSE*, *HST* and *IUE* data presented in this paper were obtained from the Multimission Archive at the Space Telescope Science Institute (MAST). STScI is operated by the Association of Universities for Research in Astronomy, Inc., under NASA contract NAS5-26555.

REFERENCES

- Acker A., Marcout J., Ochsenbein F., Stenholm B., Tylenda R., 1992, Strasbourg-ESO Catalogue of Galactic Planetary Nebulae. ESO, Garching
- Afsar M., Bond H. E., 2005, Mem. Soc. Astron. Ital., 76, 608
- Anderson L. S., 1989, ApJ, 339, 588
- Asplund M., Grevesse N., Sauval A. J., 2005, in Barnes T. G., III, Bash F. N., eds, ASP Conf. Ser. Vol. 336, Cosmic Abundances as Records of Stellar Evolution and Nucleosynthesis. Astron. Soc. Pac., San Francisco, p. 25

- Bannister N. P., Barstow M. A., Holberg J. B., Bruhweiler F. C., 2003, *MNRAS*, 341, 477
- Bianchi L., 2011, in *Proc. IAU Symp. 283*. Cambridge Univ. Press, Cambridge, in press
- Bianchi L., Garcia M., 2002, *ApJ*, 581, 610
- Bianchi L., Grewing M., 1987, *A&A*, 181, 85
- Bianchi L., Herald J., 2007, in Gómez de Castro A., Barstow M., eds, *UV Astronomy: Stars from Birth to Death*, p. 89 (ISBN: 978-84-7491-852-6)
- Bianchi L., Herald J. E., Garcia M., 2007, in Gómez de Castro A. I., Barstow M. A., eds, *UV Astronomy: Stars from Birth to Death*, p. 101 (ISBN: 978-84-7491-852-6)
- Bianchi L., Herald J., Garcia M., 2009, in van Steenberg M. E., Sonneborn G., Moos H. W., Blair W. P., eds, *AIP Conf. Ser. Vol. 1135, The Fundamental Parameters of Massive Stars*. Am. Inst. Phys., New York, p. 145
- Blöcker T., 1995, *A&A*, 299, 755
- Bouret J., Lanz T., Hillier D. J., 2005, *A&A*, 438, 301
- Bouret J.-C., Lanz T., Hillier D. J., Heap S. R., Hubeny I., Lennon D. J., Smith L. J., Evans C. J., 2003, *ApJ*, 595, 1182
- Cardelli J. A., Clayton G. C., Mathis J. S., 1989, *ApJ*, 345, 245 (CCM)
- Cassinelli J. P., Olson G. L., 1979, *ApJ*, 229, 304
- Chlebowski T., Garmany C. D., 1991, *ApJ*, 368, 241
- Chu Y., Gruendl R. A., Guerrero M. A., 2004, in Meixner M., Kastner J. H., Balick B., Soker N., eds, *ASP Conf. Ser. Vol. 313, Asymmetrical Planetary Nebulae III: Winds, Structure and the Thunderbird*. Astron. Soc. Pac., San Francisco, p. 254
- Ciardullo R., Jacoby J. H., 1999, *ApJ*, 515, 191
- Cohen D. H., de Messières G. E., MacFarlane J. J., Miller N. A., Cassinelli J. P., Owocki S. P., Liedahl D. A., 2003, *ApJ*, 586, 495
- Cohen D. H., Leutenegger M. A., Wollman E. E., Zsargó J., Hillier D. J., Townsend R. H. D., Owocki S. P., 2010, *MNRAS*, 405, 2391
- Crowther P. A., De Marco O., Barlow M. J., 1998, *MNRAS*, 296, 367
- De Marco O., Bond H. E., Harmer D., Fleming A. J., 2004, *ApJ*, 602, L93
- Fullerton A. W., Massa D. L., Prinja R. K., 2006, *ApJ*, 637, 1025
- Garcia M., Bianchi L., 2004, *ApJ*, 606, 497
- García-Díaz M. T., López J. A., García-Segura G., Richer M. G., Steffen W., 2008, *ApJ*, 676, 402
- Gayley K. G., Owocki S. P., 1995, *ApJ*, 446, 801
- Georgiev L. N., Peimbert M., Hillier D. J., Richer M. G., Arrieta A., Peimbert A., 2008, *ApJ*, 681, 333
- Goldman D. B., Guerrero M. A., Chu Y.-H., Gruendl R. A., 2004, *AJ*, 128, 1711
- Gordon K. D., Cartledge S., Clayton G. C., 2009, *ApJ*, 705, 1320
- Grosdidier Y., Moffat A. F. J., Acker A., 2003, in van der Hucht K., Herrero A., Esteban C., eds, *Proc. IAU Symp. 212, A Massive Star Odyssey: From Main Sequence to Supernova*. Astron. Soc. Pac., San Francisco, p. 192
- Guerrero M. A., Chu Y.-H., Gruendl R. A., Williams R. M., Kaler J. B., 2001, *ApJ*, 553, L55
- Guerrero M. A., Jaxon E. G., Chu Y., 2004, *AJ*, 128, 1705
- Guerrero M. A., Chu Y., Gruendl R. A., Meixner M., 2005, *A&A*, 430, L69
- Guerrero M. A., Ramos-Larios G., Massa D., 2010, *Publ. Astron. Soc. Australia*, 27, 210
- Hajian A. R., Terzian Y., 1996, *PASP*, 108, 258
- Hajian A. R., Terzian Y., Bignell C., 1995, *AJ*, 109, 2600
- Hamann W., 2010, *Ap&SS*, 329, 119
- Hamann W.-R., Koesterke L., 1998, *A&A*, 335, 1003
- Hamann W.-R., Koesterke L., Wessolowski U., 1993, *A&A*, 274, 397
- Harrington J. P., Borkowski K. J., 1994, *BAAS*, 26, 1469
- Heap S. R., 1977, *ApJ*, 215, 864
- Heber U., Drilling J. S., 1984, *Mitteilungen der Astronomischen Gesellschaft Hamburg*, 62, 252
- Heber U., Werner K., Drilling J. S., 1988, *A&A*, 194, 223
- Herald J. E., Bianchi L., 2002, *ApJ*, 580, 434
- Herald J. E., Bianchi L., 2004a, *ApJ*, 611, 294
- Herald J. E., Bianchi L., 2004b, *ApJ*, 609, 378
- Herald J. E., Bianchi L., 2007, *ApJ*, 661, 845
- Herald J., Bianchi L., 2009, in van Steenberg M. E., Sonneborn G., Moos H. W., Blair W. P., eds, *AIP Conf. Ser. Vol. 1135, Future Directions in Ultraviolet Spectroscopy*. Am. Inst. Phys., New York, p. 151
- Herald J. E., Hillier D. J., Schulte-Ladbeck R. E., 2001, *ApJ*, 548, 932
- Herald J. E., Bianchi L., Hillier D. J., 2005, *ApJ*, 627, 424
- Hillier D. J., 2008, in Hamann W.-R., Feldmeier A., Oskinova L. M., eds, *Clumping in Hot-Star Winds*. University of Potsdam, Potsdam, p. 93
- Hillier D. J., Miller D. L., 1998, *ApJ*, 496, 407
- Hillier D. J., Miller D. L., 1999, *ApJ*, 519, 354
- Hillier D. J., Lanz T., Heap S. R., Hubeny I., Smith L. J., Evans C. J., Lennon D. J., Bouret J. C., 2003, *ApJ*, 588, 1039
- Hoare M. G., Drake J. J., Werner K., Dreizler S., 1996, *MNRAS*, 283, 830
- Holberg J. B., Barstow M. A., Sion E. M., 1998, *ApJS*, 119, 207
- Holberg J. B., Barstow M. A., Sion E. M., 1999, in Solheim S.-E., Meistas E. G., eds, *ASP Conf. Ser. Vol. 169, 11th European Workshop on White Dwarfs*. Astron. Soc. Pac., San Francisco, p. 485
- Hubeny I., Lanz T., 1995, *ApJ*, 439, 875
- Hyung S., Aller L. H., 1997, *ApJ*, 491, 242
- Jordan S., Werner K., O'Toole S. J., 2005, *A&A*, 432, 273
- Kastner J. H., 2007, in Corradi R. L. M., Manchado A., Soker N., eds, *Asymmetrical Planetary Nebulae IV X-ray Emission from Planetary Nebulae and their Central Stars: A Status Report*. <http://www.iac.es/proyecto/apn4/pages/proceedings.php>
- Keller G., Herald J., Bianchi L., Maciel W., Bohlin R., 2011, *MNRAS*, in press, doi:10.1111/j.1365-2966.19085.x
- Koesterke L., Dreizler S., Rauch T., 1998, *A&A*, 330, 1041
- Kudritzki R. P., Urbaneja M. A., Puls J., 2006, in Barlow M. J., Méndez R. H., eds, *Proc. IAU Symp. 234, Planetary Nebulae in our Galaxy and Beyond*. Cambridge Univ. Press, Cambridge, p. 119
- Lame N. J., Pogge R. W., 1996, *AJ*, 111, 2320
- Leutenegger M. A., Paerels F. B. S., Kahn S. M., Cohen D. H., 2006, *ApJ*, 650, 1096
- Lucy L. B., Solomon P. M., 1970, *ApJ*, 159, 879
- McCandliss S. R., Kruk J., 2007, *ApJS*, 170, 126
- McCandliss S. R., France K., Lupu R. E., Burgh E. B., Sembach K., Kruk J., Andersson B., Feldman P. D., 2007, *ApJ*, 659, 1291
- Macfarlane J. J., Cohen D. H., Wang P., 1994, *ApJ*, 437, 351
- Marcolino W. L. F., Hillier D. J., de Araujo F. X., Pereira C. B., 2007, *ApJ*, 654, 1068
- Marigo P., Bernard-Salas J., Pottasch S. R., Tielens A. G. G. M., Wesselius P. R., 2003, *A&A*, 409, 619
- Martins F., Schaerer D., Hillier D. J., 2002, *A&A*, 382, 999
- Martins F., Schaerer D., Hillier D. J., Meynadier F., Heydari-Malayeri M., Walborn N. R., 2005, *A&A*, 441, 735
- Mendez R. H., Niemelä V. S., 1977, *MNRAS*, 178, 409
- Miranda L. F., Solf J., 1992, *A&A*, 260, 397
- Miszalski B., Acker A., Moffat A. F. J., Parker Q. A., Udalski A., 2009, *A&A*, 496, 813
- Moos H. W. et al., 2000, *ApJ*, 538, 1
- Napiwotzki R., 1999, *A&A*, 350, 101
- Oskinova L. M., Hamann W., Feldmeier A., 2007, *A&A*, 476, 1331
- Owocki S. P., Cohen D. H., 2006, *ApJ*, 648, 565
- Owocki S. P., Castor J. I., Rybicki G. B., 1988, *ApJ*, 335, 914
- Owocki S. P., Cranmer S. R., Blondin J. M., 1994, *ApJ*, 424, 887
- Palen S., Balick B., Hajian A. R., Terzian Y., Bond H. E., Panagia N., 2002, *AJ*, 123, 2666
- Pauldrach A. W. A., Hoffmann T. L., Méndez R. H., 2004, *A&A*, 419, 1111
- Perinotto M., Patriarchi P., Balick B., Corradi R. L. M., 2004, *A&A*, 422, 963
- Perryman M. A. et al., 1997, *A&A*, 323, 49
- Pottasch S. R., Bernard-Salas J., 2010, *A&A*, 517, A95
- Pottasch S. R., Beintema D. A., Bernard Salas J., Feibelman W. A., 2001, *A&A*, 380, 684
- Pottasch S. R., Bernard-Salas J., Roellig T. L., 2008, *A&A*, 481, 393

- Prinja R. K., Hodges S. E., Massa D. L., Fullerton A. W., Burnley A. W., 2007, *MNRAS*, 382, 299
- Puls J., Markova N., Scuderi S., Stanghellini C., Taranova O. G., Burnley A. W., Howarth I. D., 2006, *A&A*, 454, 625
- Raymond J. C., Smith B. W., 1977, *ApJS*, 35, 419
- Reed D. S., Balick B., Hajian A. R., Klayton T. L., Giovanardi S., Casertano S., Panagia N., Terzian Y., 1999, *AJ*, 118, 2430
- Repolust T., Puls J., Herrero A., 2004, *A&A*, 415, 349
- Schmutz W., Hamann W.-R., Wessolowski U., 1989, *A&A*, 210, 236
- Schoenberner D., 1983, *ApJ*, 272, 708
- Schonberner D., Drilling J. S., 1984, *ApJ*, 278, 702
- Schönberner D., Steffen M., 2003, in Kwok S., Dopita M., Sutherland R., eds, *Proc. IAU Symp. 209, Planetary Nebulae: Their Evolution and Role in the Universe*. Astron. Soc. Pac., San Francisco, p. 147
- Schulz N. S., Canizares C., Huenemoerder D., Tibbets K., 2003, *ApJ*, 595, 365
- Stanghellini L., Guerrero M. A., Cunha K., Manchado A., Villaver E., 2006, *ApJ*, 651, 898
- Steffen M., Schonberner D., Kifonidis K., Stahlberg J., 1997, in Habing H. J., Lamers H. J. G. L. M., eds, *Proc. IAU Symp. 180, Planetary Nebulae*. Kluwer, Dordrecht, p. 368
- Terzian Y., 1997, in Habing H. J., Lamers H. J. G. L. M., eds, *Proc. IAU Symp. 180, Planetary Nebulae*. Kluwer, Dordrecht, p. 29
- Tinkler C. M., Lamers H. J. G. L. M., 2002, *A&A*, 384, 987
- Todt H., Hamann W., Gräfener G., 2008, in Hamann W.-R., Feldmeier A., Oskinova L. M., eds, *Clumping in Hot-Star Winds*. University of Potsdam, Potsdam, p. 251
- Traulsen I., Hoffmann A. I. D., Rauch T., Werner K., Dreizler S., Kruk J. W., 2005, in Koester D., Moehler S., eds, *ASP Conf. Ser. Vol. 334, 14th European Workshop on White Dwarfs*. Astron. Soc. Pac., San Francisco, p. 325
- Wehmeyer R., Kohoutek L., 1979, *A&A*, 78, 39
- Weinberger R., 1989, *A&AS*, 78, 301
- Werner K., Herwig F., 2006, *PASP*, 118, 183
- Werner K., Rauch T., Reiff E., Kruk J. W., Napiwotzki R., 2004, *A&A*, 427, 685
- Werner K., Rauch T., Kruk J. W., 2005, *A&A*, 433, 641
- Werner K., Rauch T., Kruk J. W., 2007a, *A&A*, 466, 317
- Werner K., Rauch T., Kruk J. W., 2007b, *A&A*, 474, 591
- Werner K., Rauch T., Kruk J. W., 2008, *A&A*, 492, L43
- Zsargó J., Hillier D. J., Bouret J., Lanz T., Leutenegger M. A., Cohen D. H., 2008, *ApJ*, 685, L149

This paper has been typeset from a $\text{\TeX}/\text{\LaTeX}$ file prepared by the author.